Multiscale Probing of Colloidal Gelation Dynamics

by

Jae Hyung Cho

B.S., Mechanical Engineering
Korea Advanced Institute of Science and Technology (2016)

Submitted to the Department of Mechanical Engineering
in partial fulfillment of the requirements for the degree of

Master of Science in Mechanical Engineering

at the

MASSACHUSETTS INSTITUTE OF TECHNOLOGY

June 2018

Author ..... Signature redacted
Department of Mechanical Engineering
May 11, 2018

Certified by ..... Signature redacted
Irmgard Bischofberger
Assistant Professor of Mechanical Engineering
Thesis Supervisor

Accepted by: ..... Signature redacted
Rohan Abeyaratne
Professor of Mechanical Engineering
Chairman, Department Committee on Graduate Students

This page is intentionally left blank

Multiscale Probing of Colloidal Gelation Dynamics

by

Jae Hyung Cho

Submitted to the Department of Mechanical Engineering
on May 11, 2018 in partial fulfillment of the
requirements for the degree of
Master of Science in Mechanical Engineering

Abstract

Colloidal gels are viscoelastic materials characterized by the collective behavior of particles that form a space-spanning network. Although the network structure embodies the aggregation process of the particles, the kinetic pathway from a stable suspension to such a complex microstructure remains poorly understood. In this work, we explore the evolution of microscopic structure and dynamics of home-made colloidal particles in the early phase of gelation, by extending the applicability of Differential Dynamic Microscopy (DDM) to non-ergodic media. We demonstrate uncoupled development of the structure and dynamics that reveals an intermediate stage of gel formation, and compare the DDM results with the rheological features of evolving gels. We finally show how understanding the gelation at multiple length and time scales via DDM and rheology opens new ways to tune the mechanical properties of colloidal gels that bear inherent versatility.

Thesis Supervisor: Irmgard Bischofberger

Title: Assistant Professor of Mechanical Engineering

This page is intentionally left blank

Acknowledgements

I would like to express my sincere gratitude to Professor Irmgard Bischofberger for her guidance and support. Her care and enthusiasm as an advisor and a mentor have truly enriched my experience at MIT, and I am thrilled to continue working with her for my PhD study.

I would like to thank Professor Veronique Trappe at the University of Fribourg, Professor Roberto Cerbino at the University of Milan, and Professor James Swan of the Department of Chemical Engineering at MIT for insightful discussions.

I am grateful to my friends at Hatsopoulos Microfluids Laboratory for their support, inspiration, and boundless energy. I would also like to thank my friends outside the lab for making my life even more fun.

Finally, I would like to thank my family in Korea for making me who I am today.

This page is intentionally left blank

Contents

List of Figures and Tables

Chapter 1

Introduction

Suspensions of attractive colloidal particles spontaneously self-assemble into space-spanning non-equilibrium structures, characterized by unique mechanical properties. They exhibit viscoelastic behavior under small stress, but fluidize as the applied stress exceeds a certain threshold. When the inter-particle attractive forces are sufficiently strong such that the particles irreversibly adhere to one another, the kinetic process of aggregation is entirely diffusion-controlled: individual particles and their aggregates approach one another through their random motions. This description of network formation is called Diffusion-Limited Cluster Aggregation (DLCA) [1–3]. On the other hand, when the attractive forces are weak, particles of an aggregate continuously break their bonds with their neighbors under thermal fluctuations, allowing more extensive rearrangement of the network structure. This process is called Reaction-Limited Cluster Aggregation (RLCA) [4–6].

One distinguishing characteristic of DLCA lies in the formation of uniform-sized clusters, or largest discrete units of particle aggregates. Although gel networks appear purely random in configuration, they are composed of the clusters that induce macroscopic homogeneity in the system [1]. The internal structure of a cluster, however, displays clear heterogeneity; its density decreases, as we probe larger portions within the cluster. This decrease in density results from that the structure becomes increasingly tenuous away from its center, such that, in statistically averaged sense, the mass (M) of any sub-unit of the cluster scales as its characteristic length (L) to the power of fractal dimension (d_f), $M \sim L^{d_f}$, where $d_f = 1.75$ [3].

The structural complexity of the resulting gels manifests itself in a number of mechanical and structural characteristics. The fractality, for example, is reflected in the power law dependence of the storage modulus on the particle volume fraction in Small Amplitude Oscillatory Shear (SAOS) experiments [7], as well as in another power law behavior of the static structure factor $S(q) \sim q^{-d_f}$

over a range of wave vectors q with exponent d_f corresponding to the fractal dimension, in Static Light Scattering (SLS) [8]. Even singly bonded aggregates that comprise the network have proved capable of resisting bending torques, indicating substantial effect of tangential contact force between the particles [9], and in the limit of large amplitude shear that completely unbends and stretches the particle strands, some gels have shown strain-hardening behavior before fracture [10]. The dynamics of gel networks driven by thermal fluctuations [11] and intermittent particle rearrangements [12], measured with Dynamic Light Scattering (DLS), have revealed a vast spectrum of length and time scales involved.

Even with these pioneering works, however, we understand little about the early stage of gelation. The majority of the studies have limited their scope to fully-developed gels with a well-established percolating network of particles exhibiting steady state dynamics. Yet, the structure and the mechanical properties of the gels are entirely set by how the particles aggregate. Therefore, bringing colloidal gels into the realm of engineering by being able to tune their mechanical behavior demands understanding the physics of early kinetic pathways from a stable suspension to a gel.

In this work, we explore the microscopic evolution of structures and dynamics of a home-made colloidal system during gelation and its relation to rheological properties. The system is composed of polystyrene-poly(N-isopropylacrylamide) or PS-PNIPAM core-shell particles suspended in density-matched water. Due to the temperature sensitive dimensions of PNIPAM, we can control the gelation by adjusting the system temperature. With rheology, we observe multiple phases of gel evolution, and frequency dependence of the viscoelastic moduli of the gel. For microscopic characterization, on the other hand, we develop a new methodology to apply Differential Dynamic Microscopy (DDM) [13] to non-ergodic media, and find distinct time scales of the evolution of structures and dynamics of the gel networks. Finally, we extend the application of DDM to estimate the gel elasticity without mechanical perturbation, and start exploring the behaviors of binary mixtures of different particles to devise a way to tune the properties of colloidal gels.

Chapter 2

Experimental Methods

2.1 Preparation and description of PS-PNIPAM particles

2.1.1 Synthesis protocol and sample preparation

The polystyrene-poly(N-isopropylacrylamide) (PS-PNIPAM) core-shell colloidal particles are prepared by emulsion polymerization based on the protocol of Dingenouts et al. [14], with minor modifications on the amounts of ingredients. In a 1L flask equipped with a stirrer, a reflux condenser, and a gas inlet, 25.02 g of N-isopropylacrylamide (NIPAM; Acros Organics) and 0.2008 g of the stabilizer sodium dodecyl sulfate (SDS; Sigma-Aldrich) are dissolved in 525.14 g of DI water with stirring. After the solution is bubbled with nitrogen for 30 minutes, 142.75 g of styrene (Sigma-Aldrich) is added, and the mixture is heated to 80°C under nitrogen atmosphere. Then 0.3521 g of the initiator potassium persulfate (KPS; Acros Organics) dissolved in 15.00 g of DI water is added to the mixture being stirred. After 6 hours, the dispersion is cooled to room temperature, and cleaned through repeated centrifugation and supernatant exchange. The resulting colloids are particles with PS cores and thin PNIPAM shells.

A second set of particles with thicker PNIPAM shells is synthesized by subsequently running a seeded emulsion polymerization process after the initial polymerization. For each 100 g of the initial particles obtained, 12.58 g of NIPAM and 0.8994 g the cross-linker of N,N'-methylenebis(acrylamide) (BIS; Sigma-Aldrich) are added, and the mixture is heated to 80°C. After the addition of 0.1264 g of KPS dissolved in 9.43 g of DI water, the mixture is stirred for 4

hours, before being cooled to room temperature. The new suspension was cleaned through dialysis against DI water for approximately 4 weeks.

For both systems of particles, we prepare samples by matching the density of the solvent with that of the particles using deuterium oxide (D_2O; Acros Organics) to a final solvent composition of $H_2O/D_2O = 1.10$ vol/vol. Then 0.5 M of sodium thiocyanate (NaSCN; Acros Organics) is added to the samples to screen electrostatic inter-particle forces. We tested both systems for their dependence on the salt concentration in the range of 0.3 – 0.7 M, and observed no change in their rheological behaviors, indicating that the charges are fully screened under these conditions.

2.1.2 Characteristics of PS-PNIPAM core-shell particles

Poly(N-isopropylacrylamide) (PNIPAM) is a temperature-sensitive polymer that exhibits a lower critical solution temperature (LCST) of ~32°C, and significant changes in its dimensions even below the LCST [15]. We exploit this thermo-sensitivity of PNIPAM to tune the particle interactions in our system. At a low temperature, the PNIPAM shell is only barely thick enough to provide steric repulsion that prevents aggregation due to van der Waals attractions of the PS core. Increasing the temperature, however, reduces the thickness of the shell, such that the range of the steric repulsion decreases, which consequently leads to a deeper minimum in the interaction potential, as shown in Fig. 2.1. To ensure that the attraction is solely determined by the van der Waals interactions between the PS cores, we limit our investigations to temperatures $T \leq 30°C$, below which the intermolecular interactions of PNIPAM remain approximately constant.

The temperature sensitivity of PNIPAM enables us to control the interactions of both types of particles, but the second type, synthesized through the two-step polymerization, contains thicker PNIPAM shells that bring about longer-ranged steric repulsion, and in turn, weaker net attraction. Hence we call the particles with the thinner PNIPAM shells the strong system, and those with thicker shells the weak system hereafter.

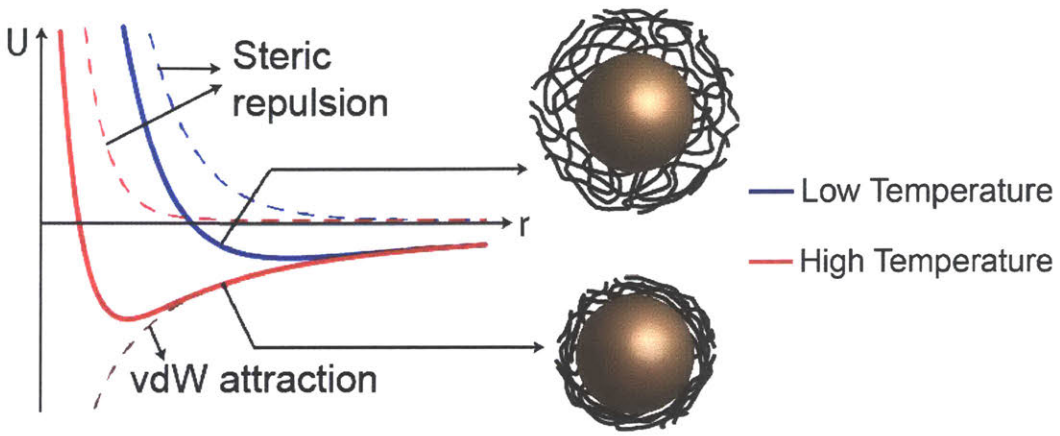

FIG. 2.1. Qualitative description of PS-PNPAM particles and their interaction potentials at low and high temperatures. At high temperature, the range of the steric repulsion is reduced, and as a result the attractive van der Waals interactions dominate, causing the particles to form aggregates. The shell size is exaggerated for clarity.

We estimate the potential depth to be approximately 30 k_BT and 5 k_BT at 30°C, for the strong and weak systems respectively, where k_B is the Boltzmann constant, and T is the temperature. This rough estimate is based on the volume fraction ϕ dependence of the shear modulus G, which exhibits a power law dependence $G = \frac{\kappa_0}{R}\phi^c$, with κ_0 the inter-particle spring constant accounting for the resistance of the bond to deformation, R the particle radius, and c a constant [11,16]; for our gels we find $c = 3.51$ and $\kappa_0 = 5.18 \times 10^{-1}$ N/m for the strong system, and $c = 3.21$ and $\kappa_0 = 2.52 \times 10^{-3}$ N/m for the weak system. We assume van der Waals interactions between PS spheres in water and estimate the magnitude of the attraction by taking the second derivative of the van der Waals potential to match the experimental value of κ_0.

The size of the PS-PNIPAM particles is determined in Dynamic Light Scattering (DLS) experiments using extremely dilute solutions of $\phi \sim 10^{-5}$. The light scattering apparatus used is BI-200SM (Brookhaven Instruments), and we use the Stokes-Einstein relation to calculate the hydrodynamic radius (R_h) of the particles.

The results for both systems of particles at 21°C to 29°C are reported in Table 2.1. The intensity autocorrelation functions measured are single exponentials, reflecting reasonable monodispersity of our particles. The smaller values of R_h at 29°C indicate that the PNIPAM shell thickness

diminishes at the higher temperature. The actual shell thickness variation, however, is presumed to be lower than the changes in R_h, as the hairy configuration of the PNIPAM shell stretching outward at the lower temperature increases the surface to volume ratio, leading to greater viscous drag.

TABLE 2.1. Hydrodynamic radius (R_h) of PS-PNIPAM particles measured in Dynamic Light Scattering (DLS). The single exponential intensity autocorrelation function indicates monodispersity of the synthesized systems, as further evidenced by the small standard deviations. The measurements are performed at scattering angles of 30°, 60°, and 90°.

Temperature	21°C	29°C
Strong system R_h (nm)	100.4 ± 1.3	90.3 ± 1.6
Weak system R_h (nm)	139.9 ± 1.7	116.3 ± 1.8

To obtain a crude estimate for the strong system of the temperature, at which van der Waals attraction starts to dominate over the steric repulsion, we perform a Small Amplitude Oscillatory Shear (SAOS) experiment with a temperature ramp from 15°C to 30°C at the rate of 1°C per minute on a stress-controlled rheometer (AR-G2; TA Instruments). The frequency and strain amplitude we use are 10 Hz and 1×10^{-4} respectively. For minimal delay in the detection of gelation, we use a sample with a high volume fraction ($\phi = 15\%$) of particles that ensures rapid percolation. This test, nonetheless, only provides a rough measure of the gelation temperature, as we expect an extremely slow aggregation process, compared to the ramp rate of 1°C per minute, near the gelation temperature, where the inter-particle potential depth is still comparable to thermal energy. The gelation temperature may also vary with ϕ, and hence a thorough determination of the gelation temperature would require ϕ as another control parameter.

The onset of sharp increase in the viscoelastic moduli and the crossover between the storage modulus G' and the loss modulus G'' occur just above 25°C, as shown in Fig. 2.2. These observations indicate that the sample starts to rheologically behave like a solid at this temperature, and we therefore identify 25°C as the gelation temperature. The moduli continue to increase with temperature beyond 25°C, because the higher the temperature, the further the PNIPAM shells

shrink, gradually decreasing the steric repulsion. Throughout our study, we intentionally keep the temperature below 32°C, the LCST of PNIPAM, to exclude any effect of the PNIPAM phase transition in water.

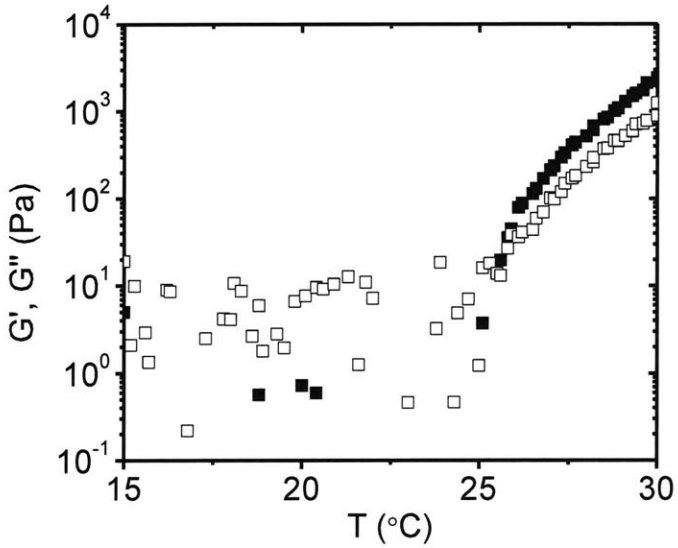

FIG. 2.2. Storage modulus (G'; solid symbols) and loss modulus (G''; open symbols) of the strong system with volume faction $\phi = 15\%$ in a temperature ramp experiment at the ramp rate of 1°C/min.

The advantage of using the PS-PNIPAM particles lies in that we have a fine control over the gelation of the system and the viscoelastic moduli in a temperature range close to room temperature. Furthermore, as the thermal response of PNIPAM is reversible, we can rejuvenate a gelled system back to a stable suspension with freely diffusing particles by readjusting its temperature below the threshold. Consequently, we obtain an excellent command over the initial conditions of our particles, as we can avoid ill-defined crude shear rejuvenation protocols typically applied to other colloids. The PS-PNIPAM particles, therefore, serve as an amenable material to investigate the transient state of colloidal gelation.

All of the following parts in this thesis, with the exception of the discussion of binary mixtures in Chapter 5, are concerned with the strong system only.

2.2 Rheological characterization

The rheological characterization of the PS-PNIPAM gels is performed on a stress-controlled rheometer (AR-G2; TA Instruments) equipped with a 40 mm diameter steel cone-plate geometry whose cone angle is 2° and truncation gap is 49 μm. The sample temperature is controlled with the lower Peltier plate of the rheometer, in the range of 15°C to 30°C. To ensure fully controlled initial conditions of each sample, we apply an extensive pre-shear as a pre-conditioning step at the rate of $\dot{\gamma} = 1000\ s^{-1}$ for 3 minutes at 15°C, below the gelation temperature, to erase any deformation history, and then wait for 2 minutes for equilibration before starting the measurement.

The characterization of the linear viscoelasticity of colloidal gels in Small Amplitude Oscillatory Shear (SAOS) experiments requires the strain amplitude to be sufficiently small to deform the system only within its linear elastic limit. Therefore, the characterization procedure is preceded by a strain sweep experiment to determine the linear amplitude regime, after rapidly raising the temperature above the gelation temperature. For gels heated to 30°C, the temperature primarily used in this study, we observe sharp increase in G' and G'' within approximately the first 300 s, followed by a slow increase over an extended period of time. We account for this by performing our oscillatory shear experiments after a precise waiting time $t = 1800$ s.

Since gels at the volume fractions of interest exhibit low moduli close to the resolution limit of the stress-controlled rheometer AR-G2, we pay greater attention to the data obtained from the weakest gels to discern artifacts. For this purpose, we refer to the criteria presented by Ewoldt et al. to determine measurement limits posed by minimum torque resolution and instrument inertia [17]. For AR-G2, the minimum applicable torque is 3 $nN \cdot m$ [18], and the instrument inertia, which includes that of the cone geometry, and is calibrated at the beginning of every experiment, is approximately 26.6 $\mu N \cdot m \cdot s^2$. The resulting minimum modulus resolution limit is $\frac{1.739 \times 10^{-4}}{\gamma_0}$ Pa, where γ_0 is the strain amplitude, and the instrument inertia limit is $2.19 \times f^2$ Pa, where f is the strain frequency in Hz. Although employed as guidelines, these criteria are not considered absolute standard for data reliability, as they are found to be rather conservative for this study.

Our protocol for gel characterization consists of three steps. At the beginning of the time sweep step after the equilibration of each sample, the temperature is increased from 15°C to 30°C, and the linear viscoelastic moduli are measured for 1800 s to observe the transient response of the colloidal system undergoing a transition from a stable suspension to a gel. The temperature increases beyond 28°C, well above the gelation temperature, within the first 10 seconds, and reaches 30°C with $\pm$ 0.1°C fluctuation within the first 40 seconds. We assume this temperature change is rapid enough, compared to the gelation time scale, to neglect any influence from the delayed temperature variation from 15°C to 30°C. The frequency is set $f = 1$ Hz, and the amplitude within the range of $2 \times 10^{-3} - 2 \times 10^{-2}$, depending on the volume fraction. The conditioning and sampling times used are 3 s each.

The time sweep step is followed by a frequency sweep step that measures the frequency response of the gels. We maintain the same strain amplitude as in the time sweep step for each sample, but adopt variable sampling times such that each data point is sampled after three complete periods of oscillation at each applied frequency. The frequencies probed range from 0.1 or 0.01 Hz to 100 Hz.

Lastly, in the strain sweep step that explores linear and nonlinear behaviors of the gels, we revert the applied strain frequency to 1 Hz, retaining the same conditioning and sampling times. We gradually increase the strain amplitude from 1×10^{-5} to 10, until after gel fracture.

After the strain sweep step, the temperature is set to return to 15°C for sample rejuvenation. Throughout this procedure, the gap temperature compensation of 0.5μm/°C is applied to minimize the effect of thermal dilation of the geometry.

2.3 Principles of Differential Dynamic Microscopy

Differential Dynamic Microscopy (DDM) is a technique developed by Cerbino and Trappe that merges the power of optical microscopy and light scattering by probing dynamics of various soft materials in both real and reciprocal spaces [13]. Initially applied to a simple system of monodisperse isotropic colloidal suspensions, DDM has proved its capability to extract information over multiple length and time scales from various complex fluids, including anisotropic colloidal particles [19], liquid crystals [20], and biological systems such as bacteria [21] and actin [22]. The technique has also shown its compatibility with many forms of microscopy, such as bright-field [13,23], dark-field [24], confocal [25], and fluorescence [26].

Compared to Dynamic Light Scattering (DLS), DDM offers immediate advantages in its accessibility and throughput. Unlike DLS, which requires a laser source, an avalanche photodiode, and a goniometer in its simplest form, DDM needs only a microscope and a camera. Moreover, since DDM computes reciprocal space quantities from ordinary microscope images, it simultaneously provides real space and reciprocal space information, which had previously been accessible only with separate probing techniques. DDM also significantly reduces the amount of sample required, as the samples are typically confined in a small, thin cell or capillary tubing to be compatible with a microscope, whereas a much greater volume of samples needs be loaded in a cuvette for DLS measurements. An extensive assessment of the strengths and limitations of DDM is presented in [27].

Specifically in the analysis of colloidal gels, DDM can outperform DLS for at least three reasons. First, DDM allows more turbid samples to be examined, whereas DLS measurements necessitate extreme dilution of samples to achieve the single scattering limit, where each photon detected by the photodiode is scattered only once within the sample. This feature restricts the colloidal gels that can be studied with DLS to those at very low volume fraction, characterized by highly fragile and tenuous networks that typically take several hours or days to form. Therefore, DDM can dramatically accelerate experimental processes, and bring the regime of microscopic

characterization closer to that of macroscopic, mechanical exploration, where gels need to be strong enough to bear measurable stress.

Second, colloidal gel networks manifest heterogeneity in terms of the length and time scales observed in their structures and dynamics. Hence a DLS measurement at a specific scattering angle, corresponding to a single wave vector that sets the length scale being probed, can provide only a modicum of the rich information that such networks contain. DDM performs unrivaled, by simultaneously processing signals at multiple length scales that range over a decade of wave vectors.

Lastly, non-ergodicity of colloidal gel systems prevents convenient methods for appropriate ensemble averaging of the scattered intensity signal in DLS. Since gelation leads to kinematic arrest of colloidal particles, the system remains at a thermodynamic non-equilibrium [28], which in turn renders scattering examination of a specific narrow region within the sample inadequate for collecting statistics representative of the entire system. In other words, no matter how long one observes the fluctuation of a scattered light, one cannot comprehend the overall system behavior as long as the observation field stays unaltered; time averaging is not equivalent to ensemble averaging. Though some ingenious techniques have been reported that enable characterization of non-ergodic samples with DLS, they require a rather laborious process and additional steps in the analysis [29,30]. DDM, on the other hand, accomplishes the ensemble averaging of the signals from non-ergodic systems, simply by the following the same computation procedures as for the ergodic samples, as long as an image encompasses a sufficiently wide field of view. This non-ergodicity of colloidal gels, however, poses a fundamental challenge in analyzing and understanding scattering data obtained through any means, as will be discussed in detail in Chapter 3.

We use an inverted microscope (Eclipse TE2000-U, Nikon) and a complementary metal-oxide-semiconductor (CMOS) camera (Prime Mono 2048×2048 pixels, Photometrics) for our DDM analysis. All experiments are conducted in the bright-field, and each sample is loaded in a capillary glass cell (Vitrocom) with a path length of 100 μm. For the samples of volume fraction $\phi = 0.3\%$, we use an objective lens with magnification of 40× and numerical aperture of 0.90, and for

samples of higher volume fractions, we use an objective lens with magnification $60\times$ and numerical aperture of 1.20. For rapid and stable control over the gelation of the sample, we use a home-built temperature control stage equipped with a Peltier module connected to a PID controller (TC-720, TE Technology). The sample capillaries are mounted on the module with an optical gel (Cargille) pasted for improved thermal conductivity. Gelation process of each sample is observed by applying a rapid heating from 20°C to 30°C; the temperature stabilizes to 30 ± 0.02°C within the first 15 s, with a 5 s-long overshoot of maximal 0.7°C. All computational analyses are implemented in MATLAB.

2.3.1 Principles

The essential step in DDM is to calculate a correlation function, called image structure function, of two images separated by an arbitrary delay time Δt. After subtracting one image from the other treating them as large arrays of pixel intensity values, we can apply two-dimensional Fast Fourier Transform (2D FFT) to the difference image. Square of the modulus of the complex-valued Fourier transformed difference image then provides a spectral decomposition of the energy content (power spectrum) of intensity captured in the difference image. The resulting values in the reciprocal space represent the temporal change of intensity captured in the real space image at the corresponding spatial frequencies, each of which can be directly associated with a unique scattering vector. As a result, the accessible domain of wave vectors via DDM is limited by the image size at its lower bound, and the pixel number at its upper bound.

If we repeat this computation for all combinations of two images from the entire image stack, and if the signal captured by the camera is stationary (i.e. statistical quantities remain unchanged over the entire time scale of image acquisition), we can take averages of the spectral decomposition as a function of the time interval between the images for statistical improvement of data. A stack of N images taken at an interval time a yields $N-1$ time-averaged power spectra of difference images at $N-1$ delay times, as shown in Fig. 2.3. This enables us to probe a time span of $(N-1)a$ simultaneously at all the length scales represented by the scattering angles (spatial frequencies) included in the image.

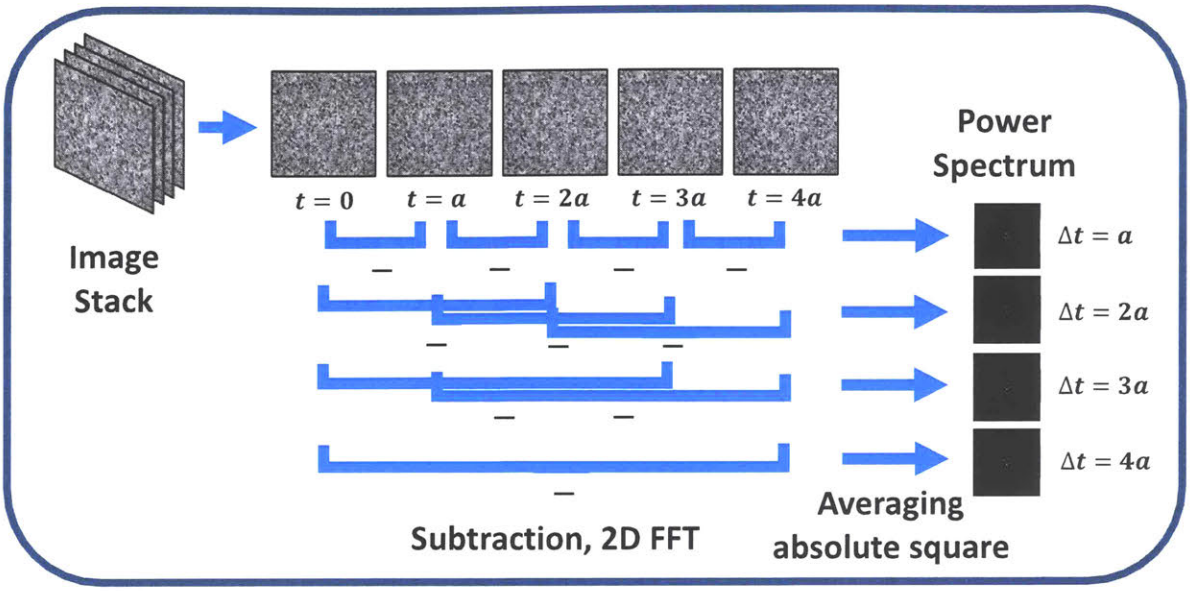

FIG. 2.3. Schematic illustration of temporal averaging procedure over the entire time scale of an image stack. Since there are fewer combinations of images separated by larger delay times Δt, the statistics become poorer for larger delay times.

For isotropic samples, the 2D power spectrum displays no directionality, and can be treated as a one-dimensional quantity in the radial direction. Thus, performing azimuthal averaging on the 2D spectrum image for every delay time Δt leads to a function that conveys information on how much an arbitrary set of two images separated by a delay time are correlated at different spatial frequencies. This function is the image structure function, here denoted by $D(q, \Delta t)$. This computation procedure to obtain the image structure function is schematically illustrated in Fig. 2.4.

The technical ground for the working principles of DDM in the framework of digital Fourier optics can be found in [31]. In this work, we use stacks of $N = 1000$ TIFF images, unless otherwise stated.

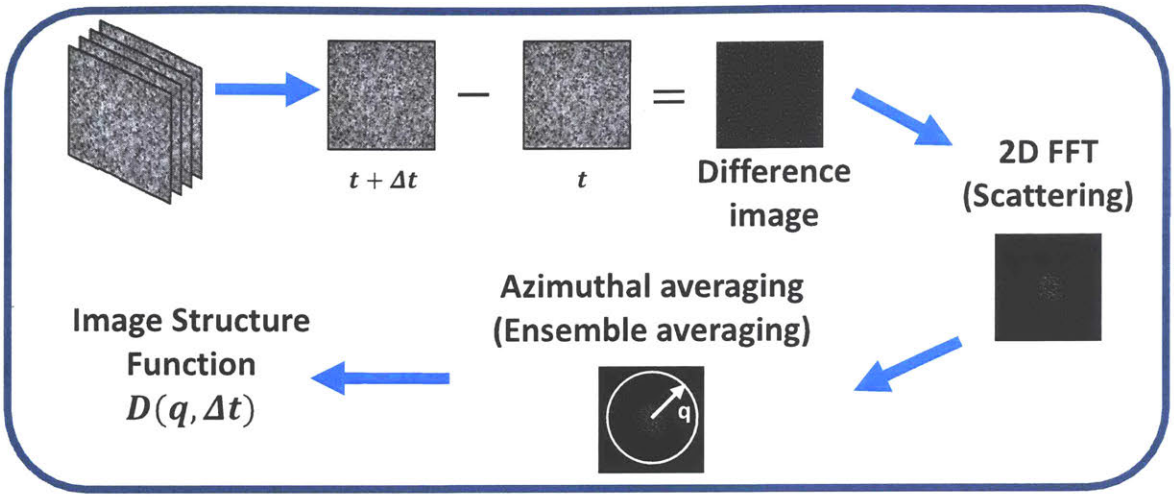

FIG. 2.4. Schematic illustration of image processing algorithm in DDM to compute image structure function. In analogy with DLS, 2D FFT is equivalent to the scattering process of light, and azimuthal averaging completes ensemble averaging.

2.3.2 DDM applied to ergodic, stable PS-PNIPAM colloidal suspensions

We verify our own code for image structure function calculation and stability of high-speed image acquisition by performing curve-fitting optimization on the image structure function obtained from the images of the ergodic, stable suspension at 20°C, below the gelation temperature.

The image structure function $D(q, \Delta t)$ can be expressed as a function of the normalized intermediate scattering function, or equivalently the dynamic structure factor $f(q, \Delta t)$, by:

$$D(q, \Delta t) = A(q)[1 - f(q, \Delta t)] + B(q). \quad (2.1)$$

$A(q)$ reflects a combined effect of optical features of the microscope, number of particles in the field of view, and static configuration of the particles, while $B(q)$ represents the contribution from camera noise [31]. $f(q, \Delta t)$ is a quantity that tells how far particles at a certain time are located with respect to the locations of all other particles at a delayed time. In DLS measurements, we obtain its value from the scattered intensity autocorrelation function [32].

For non-interacting colloidal particles at thermodynamic equilibrium, their displacements follow a Gaussian distribution, which leads to a simple exponential expression of the dynamic structure factor [33]:

$$f(q,\Delta t) = \exp\left(-\frac{\Delta t}{\tau(q)}\right). \tag{2.2}$$

Substitution of this relation into Eq (2.1) leads to the proper functional form of $D(q,\Delta t)$ for particles undergoing Brownian motion:

$$D(q,\Delta t) = A(q)\left[1 - \exp\left(-\frac{\Delta t}{\tau(q)}\right)\right] + B(q), \tag{2.3}$$

where $A(q)$, $B(q)$, and $\tau(q)$ are curve-fitting parameters to be identified. For ergodic systems, such as the stable colloidal suspension investigated here, the optimization offers robust fitting results as shown in Fig 2.5.

The image structure function obtained from the PS-PNIPAM colloidal suspension ($\phi = 0.5\%$) below the gelation temperature closely follows the simple exponential relation of Eq (2.3) at all wave vectors, and the relaxation time $\tau(q)$ obeys a power law of -2 as predicted by the Gaussian displacement distribution of non-interacting Brownian particles. Specifically, the dynamic structure factor for such systems can be expressed in terms of the mean square displacement $\langle \Delta r^2(\Delta t)\rangle$ of the particles, instead of the relaxation time as in Eq (2.2):

$$f(q,\Delta t) = \exp\left(-\frac{q^2}{4}\langle \Delta r^2(\Delta t)\rangle\right), \tag{2.4}$$

where $\langle \Delta r^2(\Delta t)\rangle$ is a linear function of the delay time Δt. The denominator 4, instead of 6, results from that DDM extracts dynamics from 2D images [23].

Since for Brownian particles, $\langle \Delta r^2(\Delta t)\rangle = 4D_0\Delta t$, where D_0 is free diffusion coefficient, we can compute the hydrodynamic radius of the particles by utilizing the Stokes-Einstein relation:

$$D_0 = \frac{k_B T}{6\pi\eta R_H}, \tag{2.5}$$

where k_B is the Boltzmann constant, η viscosity of the background fluid, and R_H the hydrodynamic radius of a particle. Yet this calculation overestimates the hydrodynamic radius of the PS-PNIPAM particles by a factor of approximately 1.5, compared to the DLS results, most likely because of the presence of unfiltered alien particles.

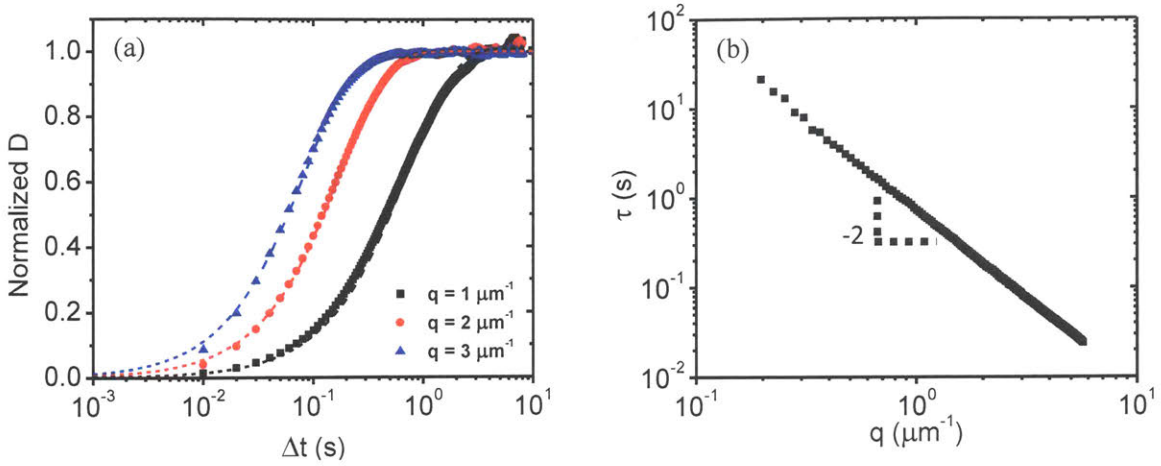

FIG. 2.5. (a) Normalized image structure function $D(q, \Delta t)$, with its exponential fits of Eq (2.3) (dashed lines) obtained from a stable PS-PNIPAM colloidal suspension at $T = 20°C$ with $\phi = 0.5\%$. Camera frame rate used here is 100 frames per second (fps), with exposure time of 10 ms. Normalized $D(q, \Delta t)$ values are shown for three different wave vectors ($q = 1$, 2, 3 μm^{-1} from right to left); larger wave vectors display faster dynamics, reducing the rise time to saturation. (b) Relaxation time $\tau(q)$ resulting from the curve-fitting, $\tau(q)$ follows a power law of -2, testifying the Brownian dynamics of the stable suspension.

Although powerful in analyzing various complex fluids including stable colloidal suspensions, this standard analysis of image structure function is inappropriate for non-ergodic solid-like systems. The gelation and the accompanying formation of the percolating network bind the particles to fixed average positions, and this constraint on the particle motion gives rise to a fundamental change in the microscopic dynamics. In Chapter 3, we discuss our extension of DDM that renders investigations of non-ergodic systems possible.

Chapter 3

Methodology development of DDM analysis on non-ergodic systems

In non-ergodic systems like colloidal gels, by definition, temporal averaging of local statistics contained in the scattered light intensity fails to offer ensemble-averaged statistics. DDM, however, collects the ensemble statistics without any extra endeavor, as long as the field of view is broad enough to capture sufficient number of clusters of the network in the images; the 2D FFT on the entire difference images and the subsequent azimuthal averaging of the power spectrum embedded in the calculation of the image structure function $D(q, \Delta t)$ ensures proper ensemble averaging of the scattered light intensity that cannot be performed with as much ease in DLS measurements. Yet the challenge arises when we attempt to extract dynamic parameters from $D(q, \Delta t)$.

3.1 Stretched exponential relaxation

One ramification of the kinematic arrest of colloidal particles through gelation is the stretched exponential relaxation. This stretched exponential relaxation necessitates modification of the functional form for the dynamic structure factor in Eq (2.2) for proper analysis of their microscopic dynamics. Fig 3.1 shows how exponential curve fitting on the computed image structure function of the PS-PNIPAM gel network ($\phi = 0.5\%$, $T = 30°C$) leads to erroneous results. The $D(q, \Delta t)$ shown for the two wave vectors are representative of $D(q, \Delta t)$ at all investigated wave vectors. $D(q, \Delta t)$ increases at slower rates than simple exponentials, and for many wave vectors, $D(q, \Delta t)$ does not saturate to a plateau within the experimental time scale.

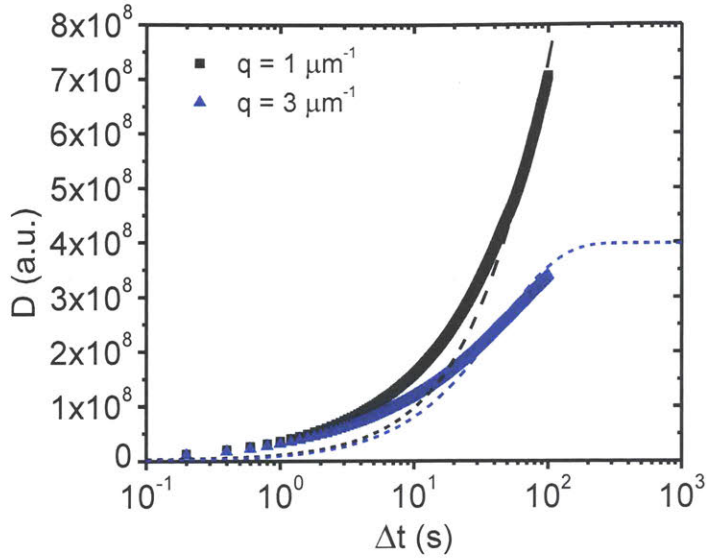

FIG. 3.1. Representative examples of image structure functions $D(q,\Delta t)$ and corresponding (poor) exponential fits shown as dashed lines at wave vectors $q = 1\ \mu m^{-1}$ (left) and $q = 3\ \mu m^{-1}$ (right) obtained from PS-PNIPAM gel network images (5 fps, $N = 500$), 15 min after the initiation of gelation at 30°C. $D(q,\Delta t)$ increases more slowly than simple exponentials, and its plateau at later delay times is often inaccessible within experimental time scales.

Such stretched exponential form of the dynamic structure factor is a well-known feature of dilute gels, whose clusters exhibit a fractal dimension $d_f = 1.9$, close to the expected value of 1.75 for DLCA gels [3]. The model proposed by Krall and Weitz interprets the motion of an individual particle in a gel network as the superposition of motions of the aggregates (and the larger aggregates of these aggregates), to which the particle is attached [11]. Thus, we can express the motion of any aggregate in a cluster as a summation, or an integral of multiple exponential terms that represent overdamped elastic modes undergoing thermal fluctuation, and this integral gives rise to the stretching exponent in the exponential term of the mean square displacement. The resulting dynamic structure factor then becomes

$$f(q,\Delta t) = \exp\left[-\frac{q^2}{6}\langle \Delta r^2(\Delta t)\rangle\right] = \exp\left[-\frac{q^2}{6}\delta^2\left\{1-\exp\left(-\left(\frac{\Delta t}{\tau^*}\right)^p\right)\right\}\right], \qquad (3.1)$$

where δ^2 is the maximum mean square displacement, τ^* the characteristic relaxation time, and p the stretching exponent, all independent of the wave vector q [11]. Krall and Weitz show good agreement between this model and experimental data for early delay times Δt.

Application of the Krall-Weitz model to the DDM analysis, however, poses practical challenges in the stabilization of the curve-fitting optimization process. Since the functional form of the dynamic structure factor proposed in Eq (3.1) contains a double exponential with multiple free parameters, we observe that the use of an automatic curve-fitting algorithm to the image structure functions at all the accessible wave vectors induces unreasonable parameter values, nullifying the high-throughput offered by DDM.

Therefore, to obtain a computationally more favorable form for the dynamic structure factor, we simplify Eq (3.1) by expanding the second exponential to the first order of the delay time Δt (which is justified for early delay times), and add an extra q-dependent term to account for the saturation of $f(q,\Delta t)$ to a non-zero plateau for large Δt. The relation then becomes

$$f(q,\Delta t) = \big(1 - C(q)\big)\exp\left[-\left(\frac{\Delta t}{\tau(q)}\right)^{p(q)}\right] + C(q), \tag{3.2}$$

where $C(q)$ is the extra parameter that leads $f(q,\Delta t)$ from its initial value of 1 to a non-zero final value. Despite the simplification, Eq (3.2) preserves the two key physical features of colloidal gel network dynamics: stretched exponential decay resulting from the hierarchy of multiple elastic modes and the incomplete decorrelation of particle positions due to the non-ergodicity. Substitution of this new relation into Eq (2.1) results in the following functional form for the image structure function that we utilize throughout this work:

$$D(q,\Delta t) = A(q)\big(1 - C(q)\big)\left[1 - \exp\left[-\left(\frac{\Delta t}{\tau(q)}\right)^{p(q)}\right]\right] + B(q). \tag{3.3}$$

3.2 Estimation of the image structure function plateau

The normalized dynamic structure factors $f(q, \Delta t)$ or equivalently the intermediate scattering functions of attractive colloidal gels obtained in both experiments [12] and simulations [34] commonly reveal two-step decays from 1 to 0 as shown in Fig. 3.2.

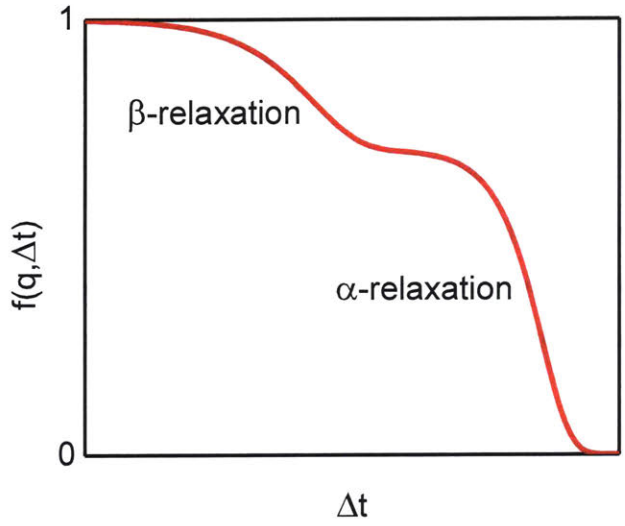

FIG. 3.2. Schematic of the two-step decay of a dynamic structure factor $f(q, \Delta t)$ at a fixed wave vector q as a function of delay time Δt.

The first decay, named β-relaxation, results from small-amplitude thermal fluctuation of the network strands, which is the relaxation accessible in this DDM analysis. The second decay, named α-relaxation, ensues the β-relaxation typically at much greater time scales, and is interpreted as a slow restructuring of the network, where particles undergo major rearrangements [35]. The difference in the time scales of these two relaxation modes uncovers itself in the form of the non-zero plateau of the dynamic structure factor after the β-relaxation.

Although we have a fair understanding of why this two-step decay of $f(q, \Delta t)$ occurs, namely the non-ergodicity originating from the kinetic arrest of colloids due to the network, we lack a priori knowledge of the time scales characterizing the onset of the intermediate plateau and its magnitude. Therefore, $D(q, \Delta t \to \infty) = A(q)\big(1 - C(q)\big) + B(q)$, the limiting value of the image structure

function at large delay times, is unknown, except that the noise term $B(q)$ is typically much smaller than $A(q)\big(1 - C(q)\big)$. Given that we typically cannot access the plateau experimentally at low q values because of the slow relaxation, obscurity of $A(q)\big(1 - C(q)\big)$ greatly compromises the quality of fit.

To aid the curve-fitting optimization, we predict $A(q)$ in advance as a guidance that provides an upper limit to the long term plateau of $A(q)\big(1 - C(q)\big)$, where $0 \leq C(q) \leq 1$. $A(q)$ is a term jointly determined by the microscope optics and the number of particles in the field of view. Specifically, $A(q)$ can be expressed as

$$A(q) = 2N\left|\hat{k}(q)\right|^2 S(q), \tag{3.4}$$

where N is the number of particles; $\hat{k}(q)$ is the transfer function, an intrinsic optical property determined by the lenses and the light source in the microscope; and $S(q)$ is the static structure factor, the static analog of the dynamic structure factor $f(q, \Delta t \to 0)$ [32].

First, $2N\left|\hat{k}(q)\right|^2$ can be obtained from the plateau of the simple exponential fit of $D(q, \Delta t)$ of the stable system at 20°C. For stable colloidal suspensions, lack of collective structures causes the static structure factor $S(q)$ to be 1, independent of q. $A(q) = 2N\left|\hat{k}(q)\right|^2$ thus holds true in Eq (2.3) for the stable system, where freely diffusive motions of particles lead to saturation of $D(q, \Delta t)$ at short delay times, as shown in Fig 2.5 (a). For the acquisition of $A(q)$ values over a large q-domain, we use one image stack file taken at a fast frame rate (100 fps), and another taken at a slow frame rate (5 fps). The resulting relaxation time from both files as a function of q, which is expected to follow a power law with exponent -2 for a freely diffusing system, is shown in Fig. 3.3. As the 100 fps image stack better captures the high q behavior, and the 5 fps image stack retains the power law in the low q regime, the combination of these sets of data produces an appropriate set of $A(q)$ over an extended q-domain.

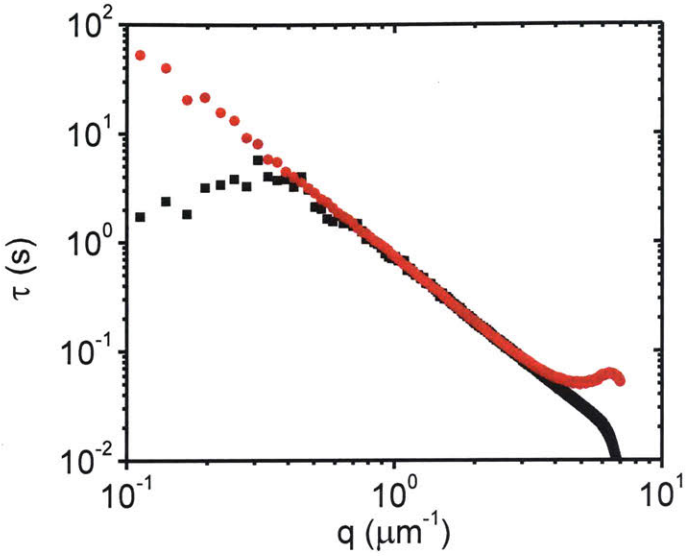

FIG. 3.3. $\tau(q)$ obtained from exponential curve fitting of $D(q, \Delta t)$ of two image stack files taken at 100 fps (black squares) and 5 fps (red circles). The two data sets follow the expected power law of -2 in different q-domains, and therefore the superposition of $A(q)$ in the high q-domain from the 100 fps file, and that in the low q-domain from the 5 fps file yields correct $A(q)$ of the stable suspensions over a large q range.

Second, $S(q)$ can be computed from the power spectrum of individual images of the gel network, rather than the difference images, averaged over the time span of the image stack files. For imaging of isotropic samples in a linear space invariant (LSI) system, the ensemble-averaged power spectrum of intensity $\langle|\hat{\imath}(q,t)|^2\rangle_E$ scales as

$$\langle|\hat{\imath}(q,t)|^2\rangle_E \sim \langle|\hat{k}(q)|^2\rangle_E \langle|\hat{c}(q,t)|^2\rangle_E, \tag{3.5}$$

where $\hat{c}(q,t)$ is the particle number density in the reciprocal space [31]. On the other hand, from the theory of conventional light scattering, we know that ensemble-averaged detected intensity $\langle\hat{I}(q,t)\rangle_E$ at a wave vector q is proportional to $\langle|\hat{c}(q,t)|^2\rangle_E$, and also independently to $S(q)P(q)$, where $P(q)$ is the form factor, a measure of scattered intensity from an individual particle:

$$\langle\hat{I}(q,t)\rangle_E \sim \langle|\hat{c}(q,t)|^2\rangle_E \sim S(q)P(q). \tag{3.6}$$

Combining Eq (3.5) and Eq (3.6) yields

$$\langle|\hat{\imath}(q,t)|^2\rangle_E = C\left|\hat{k}(q)\right|^2 S(q)P(q), \tag{3.7}$$

where C is a constant. Hence employing the fact that $S(q) = 1$ for stable systems, we can compute the static structure factor of a gel network at any age by dividing the power spectrum of gel images by that of the stable system counterpart taken before the initiation of gelation

$$\frac{\langle|\hat{\imath}(q,t)|^2\rangle_{E,gel}}{\langle|\hat{\imath}(q,t)|^2\rangle_{E,\,suspension}} = \frac{C\left|\hat{k}(q)\right|^2 S(q)P(q)}{C\left|\hat{k}(q)\right|^2 P(q)} = S(q). \tag{3.8}$$

Just as in the computation of the image structure function, $\langle|\hat{\imath}(q,t)|^2\rangle_E$ of images can be obtained from 2D FFT, calculating square norm, azimuthal averaging, and temporal averaging over all the frames in the image stack. It should be noted that this derivation assumes non-evolving behavior of the sample (i.e. sample does not evolve within the period of image acquisition), and the transfer function $\hat{k}(q)$ stays the same before and after the onset of gelation. The transfer function, in fact, may vary because of thermal dilation of the temperature control stage in our experiments, but we believe its influence on our data to be minimal.

Finally, we calculate $A(q)$ of the image structure function of gel network images:

$$A(q)_{gel} = 2N\left|\hat{k}(q)\right|^2 S(q)_{gel} = A(q)_{suspension} \cdot S(q)_{gel}. \tag{3.9}$$

The a priori knowledge of $A(q)$ with the modified fitting function of $D(q,\Delta t)$ indeed improves the quality of fit as presented in Fig. 3.4.

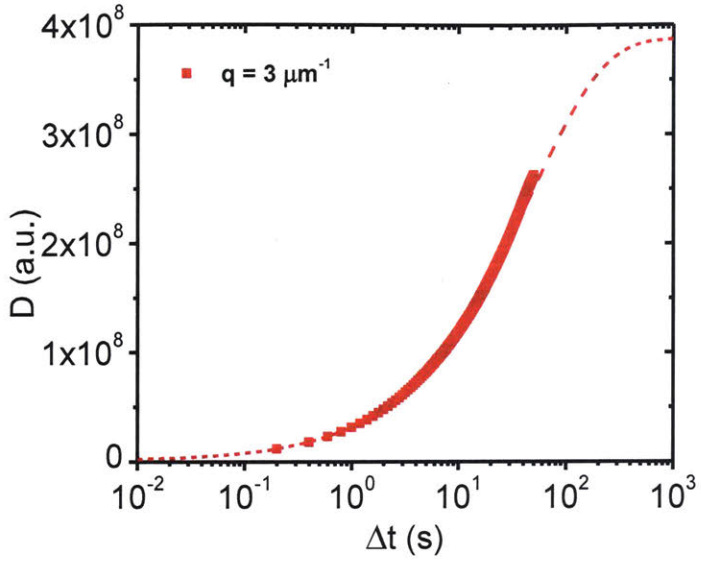

FIG. 3.4. Example of an improved fit of the image structure function $D(q, \Delta t)$ obtained from gel network images. The stretching exponent allows extra flexibility, and $A(q)$ calculation from individual images guides the fitting curve to a plateau at later times, in the absence of plateau given by the data.

3.3 Curve-fitting scheme details

Since the fitting function Eq (3.3) involves four free parameters and $D(q, \Delta t)$ calculation from microscope images offers values for restricted time scales, the choice of an initial set of parameter values for optimization requires discretion. We repeat Eq (3.3) with the free parameters color coded in red for clarity. *lsqcurvefit* function in MATLAB is used throughout.

$$D(q,\Delta t) = A(q)\big(1 - C(q)\big)\left[1 - \exp\left[-\left(\frac{\Delta t}{\tau(q)}\right)^{p(q)}\right]\right] + B(q). \tag{3.3}$$

First, given that the stretched exponential relaxation model remains valid only for the early delay times Δt [11,36], we select a proper domain of Δt for fitting by gradually increasing the Δt domain with arbitrary initial parameter values, until we observe saturation of $\tau(q)$ over an empirically

determined q-domain (approximately $0.1\ \mu m^{-1} \leq q \leq 6\ \mu m^{-1}$). If the chosen fitting domain is too narrow, we observe a severe decrease of $\tau(q)$ over the entire q-domain. If the domain is defined to be too broad, the noise becomes amplified. During this initial step of increasing the Δt domain, we find that saturation of $\tau(q)$ near its peak was not necessary as it recovers in a later step, as long as the saturation is achieved at both ends of the q-domain.

Within the chosen delay time domain, we then adjust the initial value of $C(q)$ between 0 and 1 to obtain the largest possible coincident q-domain of constant $p(q)$ and $C(q)$. After taking the mean of both $p(q)$ and $C(q)$ over the q-domain, we fix the corresponding parameters to these means, and iterate the curve-fitting optimization with only $\tau(q)$ and $B(q)$ as free parameters. The noise term $B(q)$ is always set to be less than 0.1% of the $A(q)$ value at each wave vector q. This step consistently produces noise-free trends for $\tau(q)$ with a satisfactory quality of fit.

Keeping the resulting $\tau(q)$ the $p(q)$ constant, we then repeat the curve-fitting optimization with $B(q)$ and $C(q)$ as free parameters to yield monotonically decreasing values of $C(q)$ with q. The key difference in this final optimization is that we perform curve-fit to about 80% of the total delay time domain of the entire image stack, for best estimation of the plateau location. For the image stack files with longer acquisition times, however, it is necessary to ensure the domain of fit does not capture the α-relaxation regime for high wave vectors.

Chapter 4

Results and discussion

4.1 Rheological properties of PS-PNIPAM colloidal gels

4.1.1 Gel formation: Asymptotical evolution of viscoelastic moduli

One of the main advantages of using colloids with temperature dependent attractions is that we can induce their aggregation by a temperature increase, thereby avoiding the use of an ill-defined shear rejuvenation procedure to control the history of the sample. We rapidly increase the temperature T of our suspension of PS-PNIPAM particles from 15 to 30°C. At 15°C the particles are fully dispersed, and at 30°C they interact with an attraction strength of ~30 k_BT.

Upon the sharp increase in temperature at $t = 0$ s, the system becomes unstable and the particles aggregate, which results in the formation of a stress-bearing network, as evidenced by the development of the storage modulus G' and the loss modulus G'' shown in Fig. 4.1 (a). For all the volume fractions studied here, ranging from $\phi = 1\%$ to $\phi = 15\%$, both G' and G'' steeply rise by several orders of magnitude during the first 200 s after the initiation of gelation, and then very slowly increase over an extended period of time. We hold the strain amplitudes constant ($\gamma_0 = 2 \times 10^{-3} - 2 \times 10^{-2}$) for each ϕ, ensuring that γ_0 falls within the linear elastic regime, and apply a single frequency of 1 Hz for all ϕ's.

For closer inspection of the earliest phase of the gelation, the same time evolution of the moduli is presented on log-log scale in Fig. 4.1 (b). The higher ϕ is, the earlier both moduli display the onset

of the sharp increase, and the larger their magnitude. All the samples exhibit initial latent periods, during which both moduli remain nearly constant, and the duration of the latency shortens for higher ϕ. Although the finite rate of heat transfer from the rheometer to the sample may delay the gelation, we expect that this latency also shows inherent properties of the samples, as the recorded temperature exceeds 28°C, well above the gelation temperature at 25°C, within the first 10 s, and the truncation gap is only 49 μm. The crossover between G' and G'', on the other hand, occurs after the sharp moduli increase, except for the gel with the lowest $\phi = 1\%$.

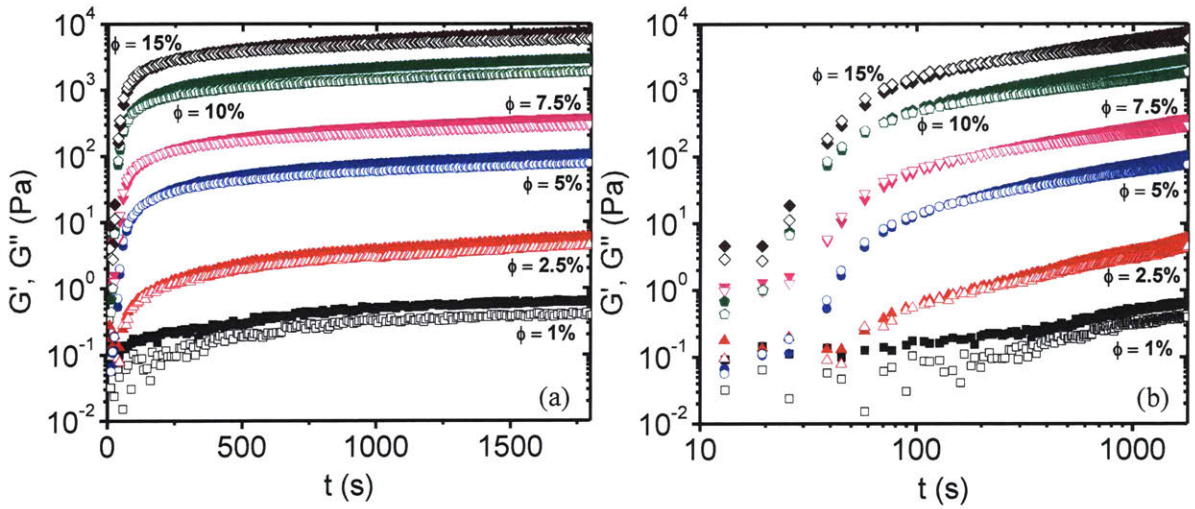

FIG. 4.1. Evolution of storage G' (solid) and loss G'' (open) moduli of PS-PNIPAM gels of different ϕ in (a) the log-linear scales and (b) the log-log scales after the sudden increase of temperature from 15°C to 30°C at time $t = 0$ s.

These two transitions may indicate that the simple description of the DLCA model fails to capture a critical evolution stage of nascent colloidal gels. The DLCA gelation time, or the time of percolation, t_g for $\phi = 1\%$ and $\phi = 15\%$ are estimated to be 9.51 s and 0.01 s, respectively, by the expression

$$t_g \approx \left(\frac{a^3\eta}{k_B T}\right)\phi^{\frac{3}{d_f-3}}, \tag{4.1}$$

where a denotes the particle radius, η the solvent viscosity, and d_f the fractal dimension of the clusters [37]. Clearly, both the end of latency and the moduli crossover, which significantly alter the mechanical behavior of the system, are observed much later than the predicted t_g.

In Fig. 4.2, we show $\tan(\delta) = G''/G'$ of the same data sets, which provides a measure of the ratio of fluid-like to solid-like behavior of the gel. Except for the data for $\phi = 1\%$, at which the gel is too weak to yield robust measurement results, $\tan(\delta)$ drops from a value higher than 1 to values below 1, as represented by the crossover between G' and G'' in Fig. 4.1 (a, b). Then all of the data sets start to reach plateaus in the range of 0.6 – 0.9, seemingly independent of ϕ, at around 750 s after the initiation of gelation. This saturation of $\tan(\delta)$ again sets a separate time scale of colloidal gelation that we cannot otherwise find in the rheometric measurements. The rather high values of the $\tan(\delta)$ plateaus indicate important viscous dissipation processes in the gels occurring at the used oscillation frequency of 1 Hz.

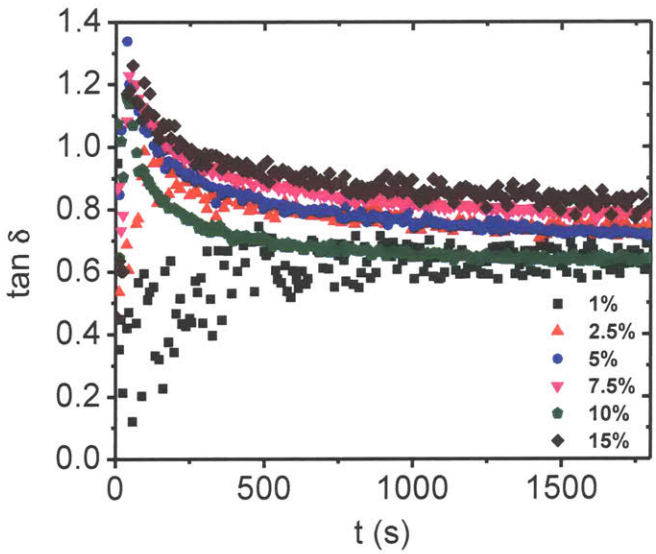

FIG. 4.2. Temporal evolution of $\tan(\delta)$ of PS-PNIPAM gels with different ϕ after the intiatiation of gelation at $t = 0$ s. For all ϕ, $\tan(\delta)$ saturates to a plateau between 0.6 and 0.9.

4.1.2 Yielding behavior

To investigate the range of linear elasticity and the yielding behavior of the PS-PNIPAM colloidal gels, we perform a series of strain sweep experiments after letting the samples evolve for 30 min at 30°C, for different volume fractions ϕ. At low strain amplitudes γ_0, the moduli of the gels are independent of γ_0 as shown in Fig. 4.3; these plateaus indicate the regimes of linear viscoelastic response. With increasing ϕ, the upper bound of the linear regime decreases as the gel becomes stiffer and more brittle. Although the limit of linearity is expected to exhibit a power law as a function of ϕ for particles possessing strong attractive forces [7], ambiguity in the exact location of the limit renders the resulting power law rather arbitrary. While the decrease in the moduli with amplitude defines the onset of nonlinear response, the crossover between storage and loss moduli marks fracture of the gel network. After the crossover, the loss modulus G'' dominates the storage modulus G', and the system rheologically behaves fluid-like, hinting at the breakage of the underlying stress-bearing network. Unlike the limit of linearity, the location of crossover does not display any obvious trend as a function of ϕ.

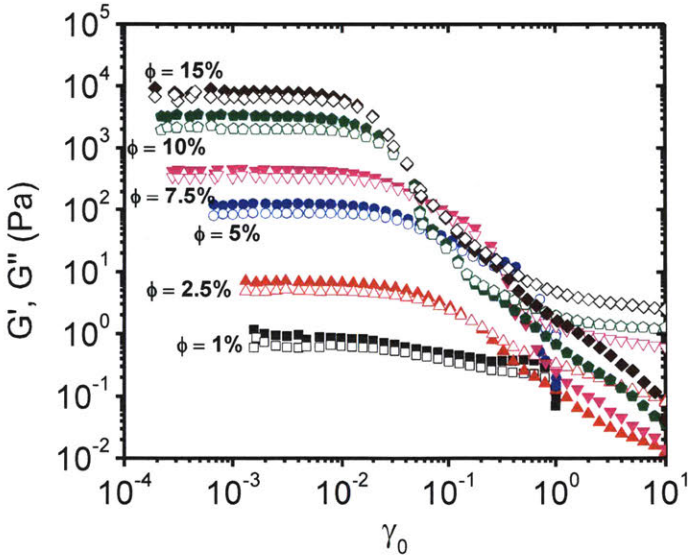

FIG. 4.3. Storage (solid) and loss (open) moduli of PS-PNIPAM gels of different ϕ with increasing strain amplitude γ_0, 30 min after the onset of gelation at 30°C.

4.1.3 Volume fraction independent frequency response

To gain further insight into the dependence of our gels on ϕ, we investigate their behavior in a range of frequencies f of the applied oscillatory shear. We let the gels evolve for 30 min at 30°C before starting the measurements. Here, the strain amplitude γ_0 is fixed to a value within the respective linear regime for each ϕ, to exclude any nonlinear effect.

Both G' and G'' moderately increase with frequency for all the volume fractions, as presented in Fig. 4.4 (a). Although the magnitudes of the moduli differ by several orders of magnitude for different ϕ, we observe that the data can be scaled onto a master curve by normalizing both moduli by the crossover modulus G^* and the frequency by the crossover frequency f^*, as shown in Fig. 4.4 (b).

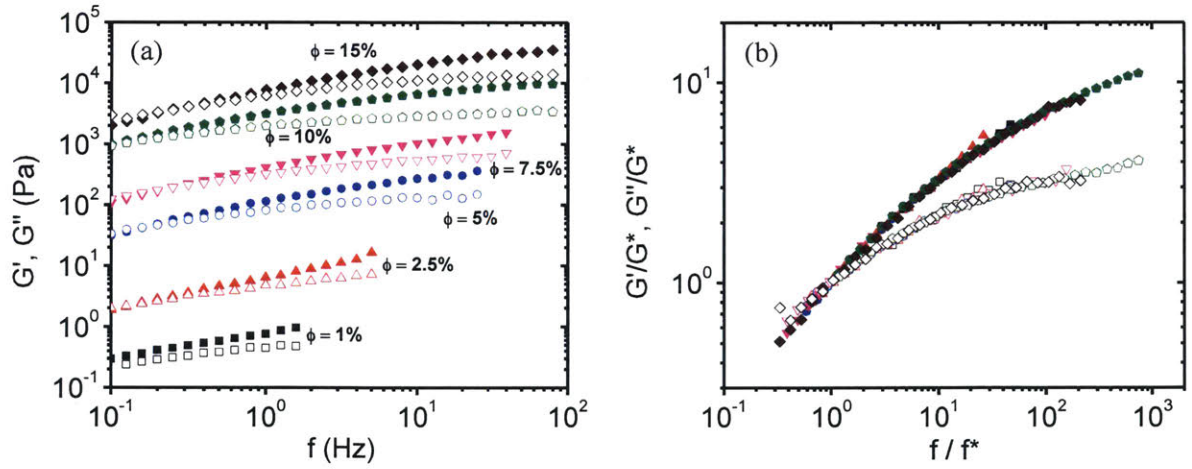

FIG. 4.4. (a) G' (solid) and G'' (open) of PS-PNIPAM gels 30 min after the beginning of gelation at 30°C as a function of strain frequency. The moduli exhibit a moderate frequency dependence for the samples with ϕ ranging from 1% to 15%. (b) Master curve resulting from the scaling of all the data in (a) by the respective crossover values.

The scaling modulus G^* exhibits a power law behavior as a function of ϕ over a decade, with an exponent of 3.81, comparable to the power law exponent of 3.28 modelled for theoretical DLCA gels at low volume fractions, as shown in Fig. 4.5 (a) [7]. This scaling behavior suggests that the PS-PNIPAM colloidal gel forms a fractal microstructure. Despite the strong inter-particle

attraction ($\sim 30k_BT$) at 30°C, the resulting gels relax at experimentally accessible frequencies, as marked by the crossover between G' and G''. The observation of the crossover indicates that the gels behave fluid-like at frequencies below the crossover frequency, indicative of slow network reconfigurations. This type of frequency response is reminiscent of the Maxwell model of viscoelastic fluids [38]. Most remarkably, the scaling frequency f^* is independent of ϕ, as shown in Fig 4.5 (b).

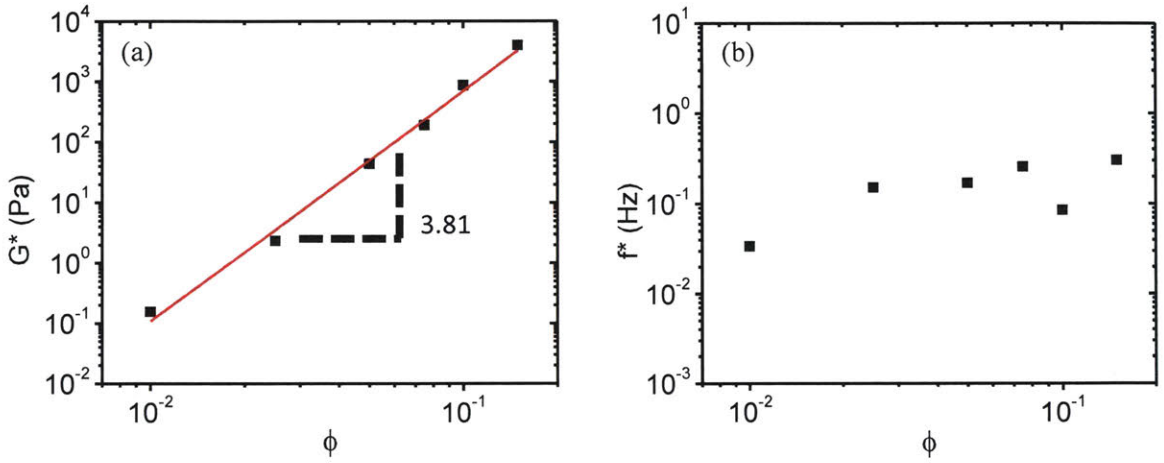

FIG. 4.5. (a) The scaling modulus G^* exhibits a power law behavior with ϕ, with exponent 3.81. (b) The scaling frequency f^* is independent of ϕ.

Understanding the scaling behavior and ϕ-independence of the frequency response as well as the multifaceted initial development of PS-PNIPAM colloidal gels revealed through the time sweep experiments calls for an exploration of their physical mechanisms. Rheological approaches, however, cannot discern the signs of these mechanisms, as a rheometer measures the bulk mechanical properties only. In the following sections, we employ DDM to seek for the hints of the physical mechanisms responsible for these rheological phenomena by investigating the microscopic structure and dynamics of the gel networks.

4.2 Microscopic structure and dynamics of PS-PNIPAM colloidal gels probed with Differential Dynamic Microscopy

4.2.1 Real space images: qualitative assessment

The change in the microstructure of the gel network during gelation is prominent in the microscope images. The PS-PNIPAM colloidal gels undergo strong configurational evolution after the rapid increase of temperature from 20°C to 30°C at $t = 0$ s, as shown in Fig. 4.6 for a gel at $\phi = 0.5\%$. The images visualize the network composed of particles of a diameter below the diffraction limit of an optical microscope from the very beginning of the aggregation process. As the gelation proceeds, we observe a gradual development of the structure as the constituents of various sizes undergo aggregation and compaction processes. We do not observe any evidence of the detachment of particles or their aggregates throughout the experiment, which suggests that the aggregation is an irreversible process, consistent with the DLCA description and our rheological findings.

Upon gelation, the particles and clusters undergo kinetic arrest within the space-spanning gel network, as evidenced by the observation that specific features of the network retain their locations within the images throughout the gelation process, despite thermal fluctuations. This finding indicates that a percolating structure pins its components, such as the particles, clusters, and sub-clusters, to fixed positions, giving rise to the non-ergodicity of the system.

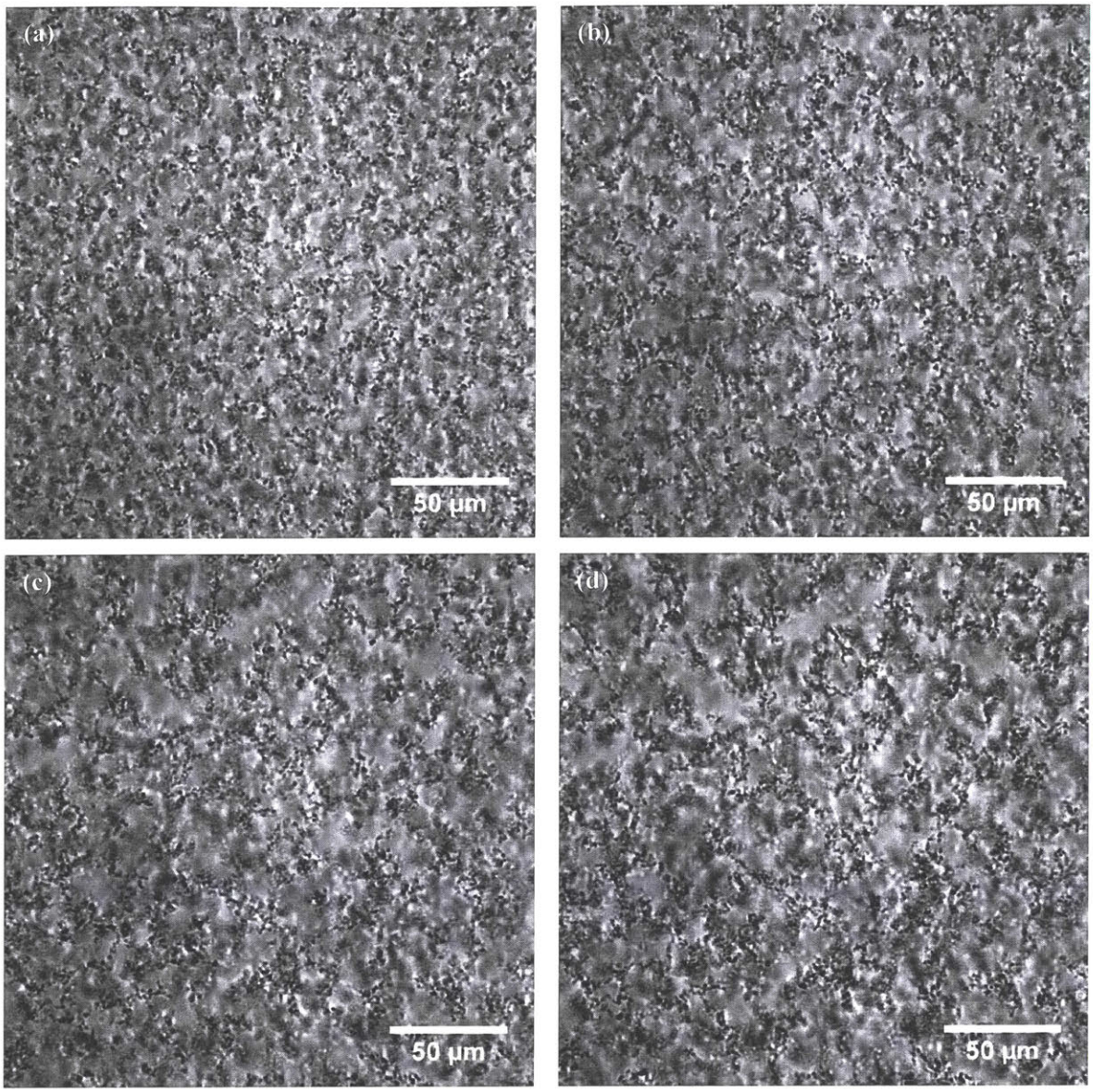

FIG. 4.6. Microscope images of the PS-PNIPAM colloidal gel ($\phi = 0.5\%$) taken (a) 2 min, (b) 5 min, (c) 15 min, (d) 30 min after the initiation of gelation by steep temperature increase from 20°C to 30°C. The texture clearly coarsens as the gel ages, as a result of aggregation and compaction.

The gel network images of the PS-PNIPAM colloidal gels further display that the grain size decreases with increasing ϕ, as presented in Fig. 4.7, for gels at four different volume fractions ($\phi = 0.3\%$, 0.5%, 0.8%, and 1.0%), 30 min after the initiation of gelation. The diminishing sizes of the aggregates elucidate that individual clusters are constrained from growing as their surroundings become more crowded.

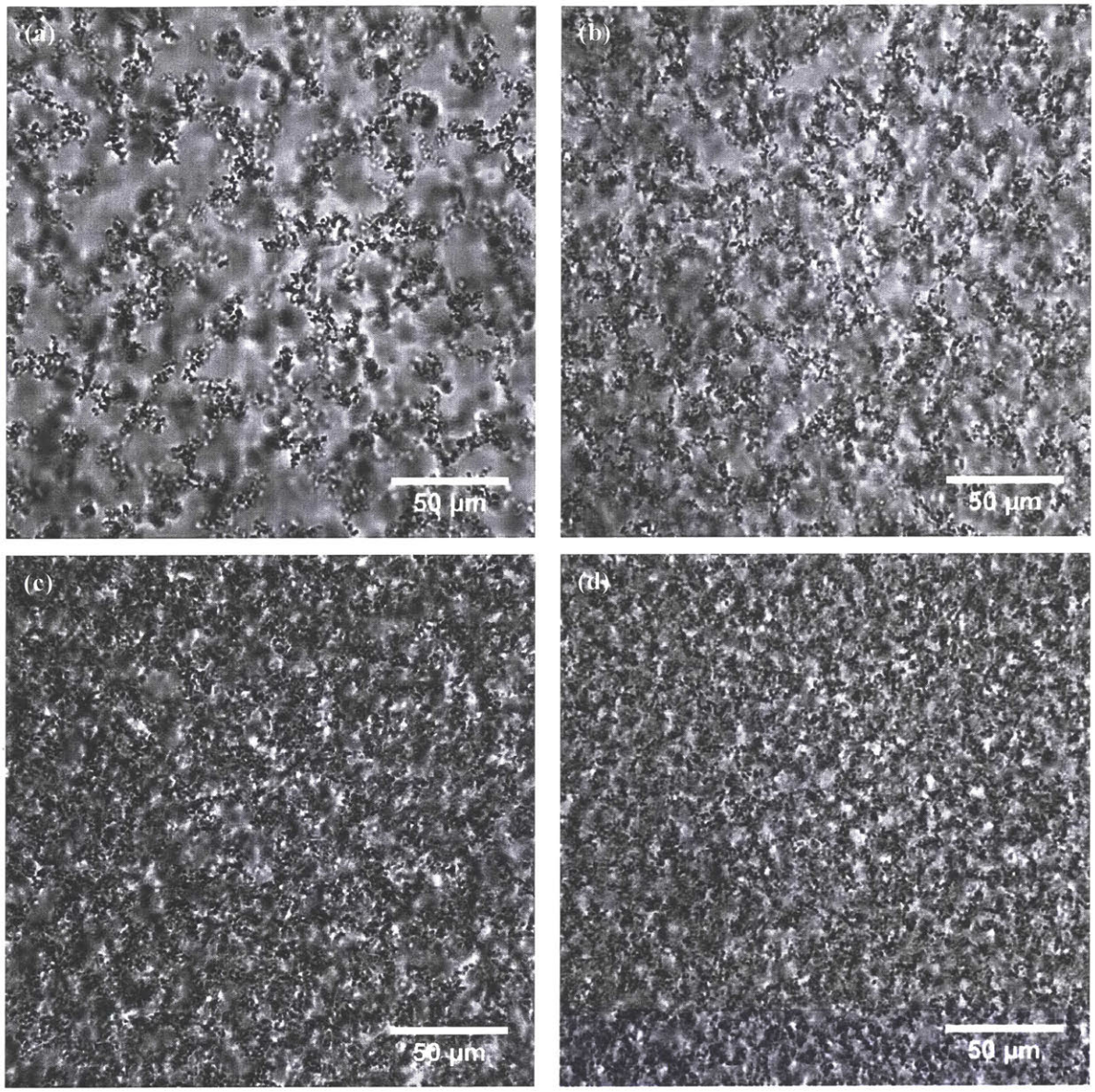

FIG. 4.7. Microscope images of the PS-PNIPAM colloidal gels with particle volume fraction ϕ of (a) 0.3%, (b) 0.5%, (c) 0.8%, (d) 1.0%, 30 min after the initiation of gelation by steep temperature increase from 20°C to 30°C. The texture coarsens with decreasing ϕ, leaving more room for the constituents to grow in size.

4.2.2 Evolution of structural properties

The implementation of 2D FFT, square norm calculation, and subsequent azimuthal and temporal averaging on the gel network images, as described in Chapter 3, allows us to quantify these visual observations. The static structure factor $S(q)$, which encodes the statistical picture of the structural characteristics of the gel network, exhibits a systematic evolution as a function of the gel age, as shown in Fig. 4.8 for a gel with $\phi = 0.5\%$ at 30°C.

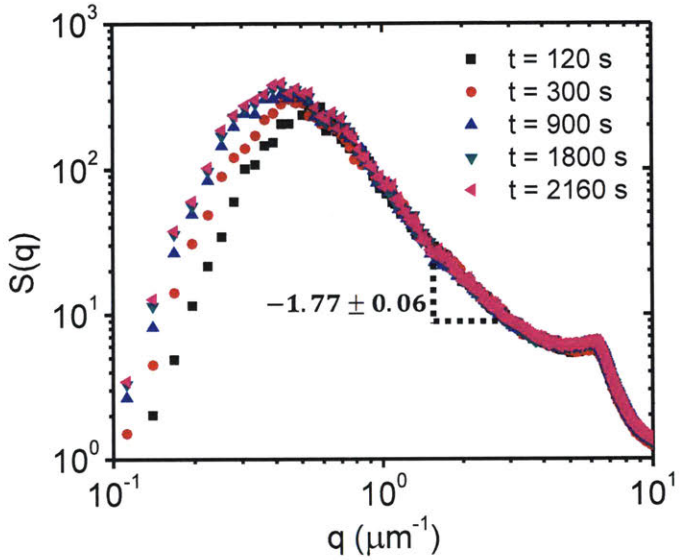

FIG. 4.8. Evolution of the static structure factor $S(q)$ during the gelation of PS-PNIPAM particles ($\phi = 0.5\%$) at $T = 30$°C. The power law shown provides the fractal dimension of the clusters.

$S(q)$ provides a measure of the total mass of the scatterers at the corresponding length scale q^{-1} [37], and in our accessible q-range, we observe several structural features of the gel. In the high q regime, a time-invariant peak at $q \cong 6\ \mu m^{-1}$ occurs, which corresponds to the real space length scale of $r = \frac{\pi}{q} \cong 500$ nm, and therefore reflects the nearest neighbor correlation between adjacent individual particles.

Over the q regime of $0.9\ \mu m^{-1} \leq q \leq 3\ \mu m^{-1}$, $S(q)$ exhibits an age independent power law behavior, a signature of scale-invariance or fractality of the microstructure [37]. The slope in the

q-domain of 1.5 $\mu m^{-1} \leq q \leq 3\ \mu m^{-1}$ is approximately -1.77, suggesting that the gel network possesses a fractal dimension of 1.77, in close agreement with that of a DLCA gel (1.75) [3]. In the q-domain of 0.9 $\mu m^{-1} \leq q \leq 1.5\ \mu m^{-1}$, we observe a larger fractal dimension of ~2.37. This might be a sign of a partial compaction of the clusters at these length scales.

The peaks in the low q-domain show the spacing among adjacent clusters. The fact that these peaks are well-defined for each gel age indicates that the cluster sizes are uniform, as expected for a DLCA gelation process [8]. In addition, the position of the peak shifts to lower q during the gelation, implying the growth of the clusters.

To estimate the cluster radii at different ages, we exploit the self-similarity of the structure to scale $S(q)$ for each gel age such that the cluster peak is located at (1,1) in the scaled coordinates as shown in Fig. 4.9 (a). The cluster radius ($R_c = \pi/q_{peak}$) increases in the early stage of gel formation as shown in Fig. 4.9 (b). q_{peak}, the location of the peak at each gel age is equal to the horizontal shift factor q^*.

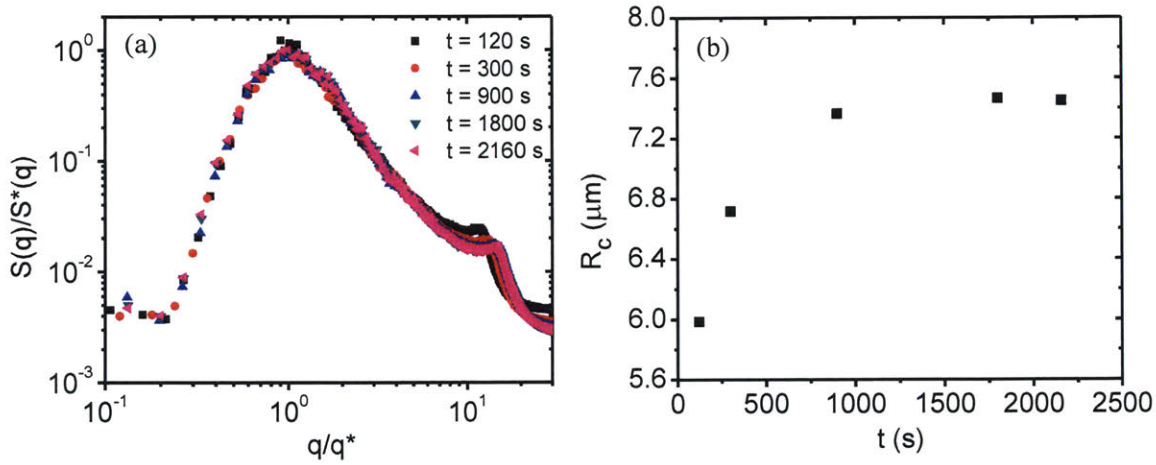

FIG. 4.9. (a) $S(q)$ of PS-PNIPAM particles ($\phi = 0.5\%$) at $T = 30°C$ scaled with the global peak located at (1,1). The deviations in the high q-domain are attributed to the spacing among individual particles that does not scale with the cluster size. (b) Cluster radius ($R_c = \pi/q_{peak}$) as a function of gel age t, where $q_{peak} = q^*$ is the wave vector corresponding to the global peak location, and is determined from the horizontal shift factor in the dynamic scaling of (a).

We find similar overall structural characteristics for all volume fractions we investigate, as demonstrated by the markedly clear scaling of all our $S(q)$ curves for different ϕ at different ages shown in Fig. 4.10.

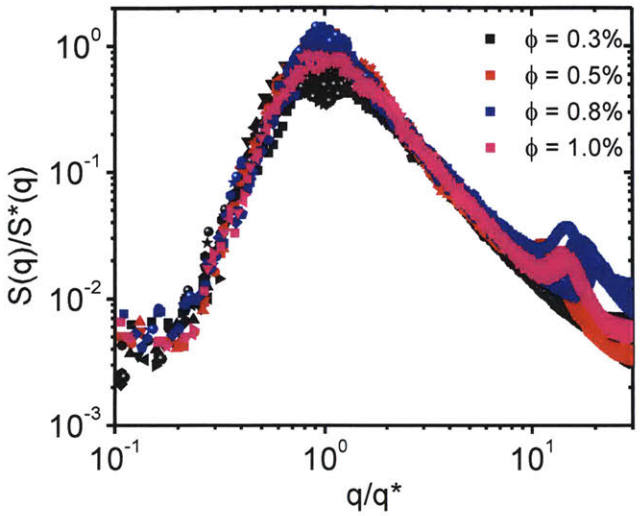

FIG. 4.10. Scaled $S(q)$ at $T = 30°C$ with the global peak located at (1,1) for four different ϕ (0.3, 0.5, 0.8, 1.0%) at different ages.

For all volume fractions, the final cluster radii of our gels differ from the theoretical DLCA prediction of

$$R_c = a\phi^{\frac{1}{d_f-3}}, \tag{4.2}$$

marked with dashed lines in Fig. 4.11 [37]. The measured cluster sizes are in general higher than the predicted values, and exhibit notably weaker ϕ dependence than predicted in Eq. (4.2). For $\phi = 0.8\%$, in particular, R_c further disobeys the model by maintaining values comparable to those of $\phi = 0.3\%$ throughout the gelation. We do not yet fully understand what induces these discrepancies between the experiments and the theoretical estimates, but they are a strong indication that the DLCA model does not accurately capture all the structural features of our colloidal gels. They might partially result from the compaction of clusters before percolation, which eventually allows each of them to occupy larger spaces upon percolation. Alternatively, they might stem from the rearrangement of particles driven by a stress field after the percolation.

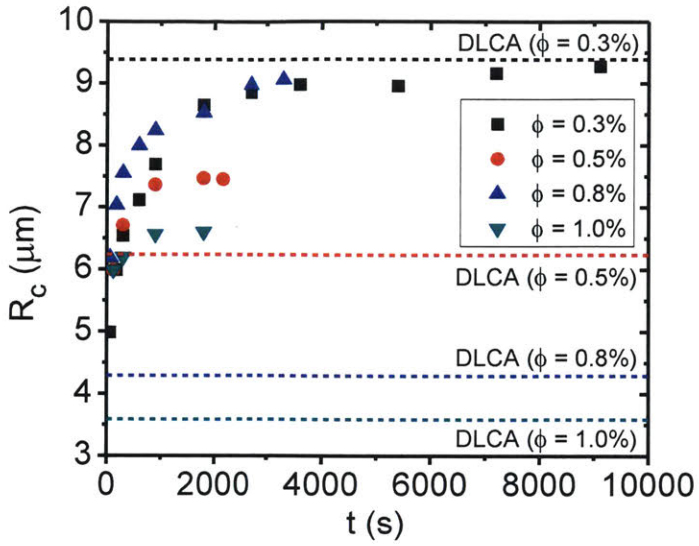

FIG. 4.11. Cluster size (R_c) as a function of gel age for $\phi = 0.3\%$, 0.5%, 0.8%, and 1.0% at $T = 30°C$. The dashed lines correspond to the theoretical DLCA gel cluster size for each ϕ.

4.2.3 Evolution of dynamic properties

In addition to the rich information on the structural evolution of gel networks that $S(q)$ delivers, DDM allows us to extract previously inaccessible data on the dynamics from the two curve-fitting parameters $\tau(q)$ and $p(q)$. These parameters give insight into new aspects of the gelation, revealing that the evolution of the gel network dynamics occurs over much longer time scales than those of the static structure.

For the PS-PNIPAM sample of $\phi = 0.5\%$ at $T = 30°C$, the characteristic time scale, or the relaxation time, $\tau(q)$ in Eq. (3.3) at different gel ages is shown in Fig. 4.12. The exponential relaxation time for the stable suspension at $T = 20°C$ before the gelation is included for reference. The power law with exponent -2 over the entire q-domain exhibited by $\tau(q)$ of the stable suspension at $t = 0$ s signifies the diffusive motion of the particles before the gelation. Upon the

initiation of gelation, however, the stretched exponential relaxation time $\tau(q)$ exhibits a peak at the values of q, corresponding to q_{peak} of $S(q)$ at each gel age.

Compared to the diffusive relaxation time scale, $\tau(q)$ during the gelation increases by three or four orders of magnitude over the q-domain corresponding to the cluster size and all smaller length scales (higher q values). On the contrary, for the lower q-domain, the increase in $\tau(q)$ is moderate, and for the lowest q values probed, and hence for the largest real space length scales, the relaxation is faster than the Brownian motion. We hypothesize that the faster dynamics at the inter-cluster length scales may be a signature of macroscopic fluid-like features of the gels, in agreement with the dominance of G'' over G' at low frequencies in our frequency sweep experiment discussed with Fig. 4.4.

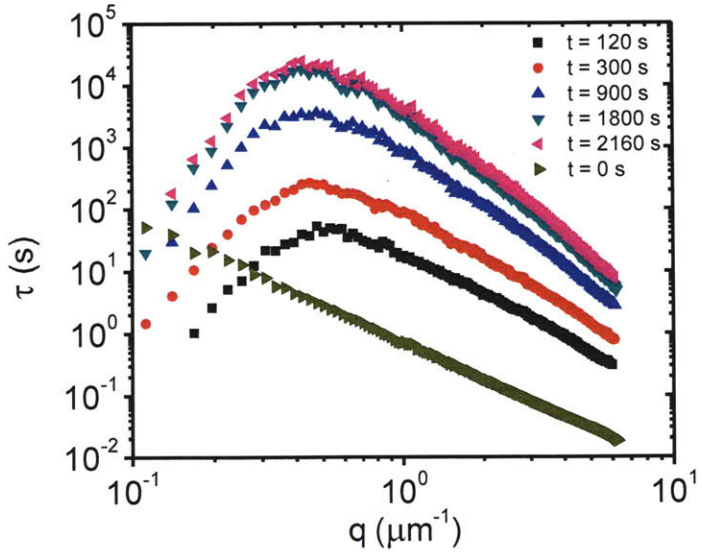

FIG. 4.12. Relaxation time $\tau(q)$ of PS-PNIPAM gel of $\phi = 0.5\%$ at different waiting times after the initiation of gelation ($T = 30°C$). The data set corresponding to the stable suspension at 20°C that exhibits a power law of -2 in the entire domain is shown for reference.

Although the static structure does not undergo any significant change after 900 s (15 min) as can be inferred from Fig. 4.9 (b), the relaxation time keeps increasing after 900 s by almost an order of magnitude over the entire q-domain. In other words, the juxtaposition of the static and dynamic information extracted via DDM explicitly discloses a phase of gelation, during which the gel

evolves dynamically, but not structurally. Yet, the dynamics parameter $\tau(q)$ indirectly exhibits embedded structural information by reaching its peak at the q values corresponding to the maximum of $S(q)$ at each gel age.

Similar characteristics of $\tau(q)$ are also observed for all other investigated volume fractions $\phi =$ 0.3%, 0.8%, and 1.0%. For denser samples with higher particle volume fraction ϕ, $\tau(q)$ at any given time is larger, as shown for the maximum of $\tau(q)$ in Fig. 4.13 (a), because of the greater kinetic constraint imposed by neighboring particles. These data points can be scaled in time as shown in Fig. 4.13 (b), implying time scale invariant behavior of aging, and the shift factors exhibit a power law as a function of ϕ with exponent -3.09 as displayed in Fig. 4.14.

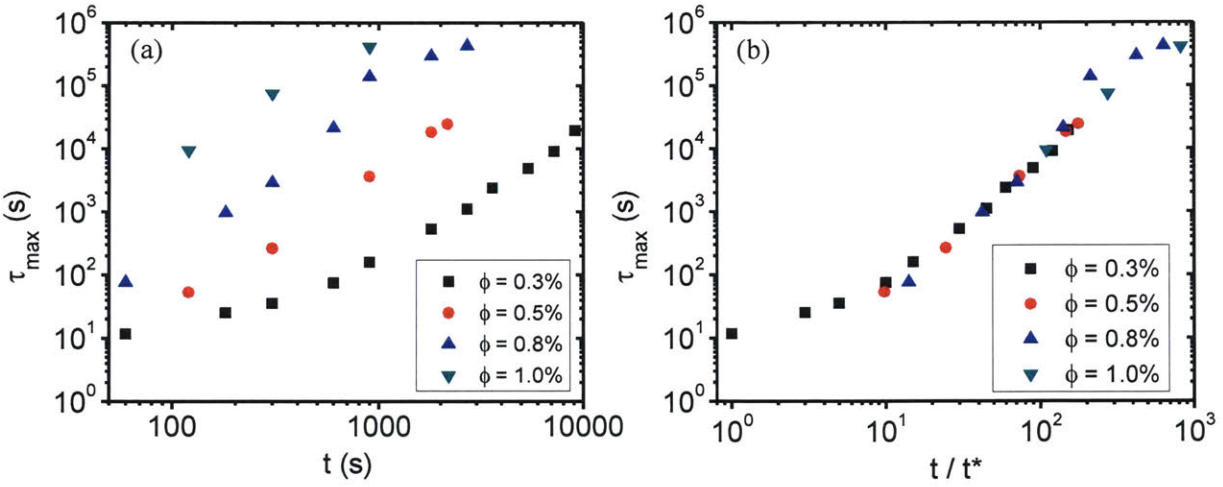

FIG. 4.13. (a) Temporal evolution of the maximum of $\tau(q)$ after the initiation of gelation of PS-PNIPAM gels with different ϕ at $T = 30°C$. (b) τ_{max} in (a) shifted horizontally such that the increasing parts for different ϕ fall onto a master curve.

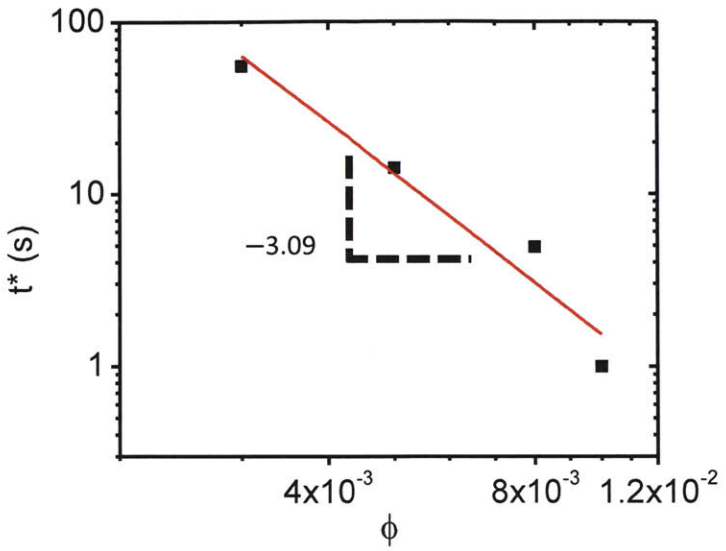

FIG. 4.14. Shift factors of τ_{max} as a function of ϕ, as obtained from the scaling shown in Fig. 4.13 (b).

For all systems regardless of ϕ, however, $\tau(q)$ continues to increase over the entire q-domain with gel age. For $\phi = 0.3\%$ at later times, the peaks of $\tau(q)$ are not as well-defined, which we speculate to result from the structural non-uniformity due to random restructuring of clusters that are allowed relatively large spaces to jiggle under thermal agitation. Note also that the largest time scales detected far exceed the image acquisition times; each image acquisition typically lasts for 10 s to 300 s, while the time scales probed throughout the gelation span eight orders of magnitude. This capacity to explore a wide range of time scales provides a comprehensive view of the heterogeneous dynamics of gelation.

The change in the stretching exponent $p(q)$ during gelation provides further insight into the evolution of the dynamics by hinting at the distributions of the different time scales that the scatterers of different length scales possess. For stable suspensions, the dynamic structure factor $f(q,\Delta t)$ follows a simple exponential decay as shown in Eq. (2.2). For thermodynamically unstable gelled systems, on the contrary, the stretching exponent $p(q)$ arises in the description of $f(q,\Delta t)$, as in Eq. (3.2). Hence, $p(q)$ is a parameter that characterizes the kinetic arrest of the particles.

Krall and Weitz first systematically developed a model to identify the stretching exponent of 0.7 as a value independent of q and ϕ that describes the fluctuations of colloidal gels [11]. To derive this exponent, the model restricts itself to the description of the internal elastic modes within a cluster, where the structure is scale-invariant (fractal). The model approximates the fluctuations at different length scales as independent, localized, overdamped oscillators, and concludes that superposition of the corresponding simple exponential relaxations of individual oscillators yields the exponent of 0.7. Romer et al., also presented experimental data on the immediate shift from a simple exponential to a stretched exponential dynamics of $p = 0.7$ upon the sol-gel transition for evolving gels at intermediate concentrations [39].

Yet, our DDM data reveal that $p = 0.7$ is not an intrinsic property of all colloidal gels as shown in Fig. 4.15 for PS-PNIPAM gels ($\phi = 0.5\%$) at $T = 30°C$. From the onset of gelation, $p(q)$, gradually decreases to a value around 0.6 after 15 min, rather than undergoing an instantaneous transition from 1 to 0.7.

Another novel feature is that $p(q)$ is independent of q, even in the low q-domain corresponding to the length scales larger than the cluster size measured from $S(q)$. This implies similar relaxation behavior on inter-cluster and intra-cluster length scales. Given that on the intra-cluster length scales the system is devoid of discrete scatterers under sub-diffusive motion that induce stretched exponential relaxation in the corresponding reciprocal space, this observation cannot be explained by the simple model of multiple elastic modes superposed in the frame of clusters as largest units that comprise the gel network.

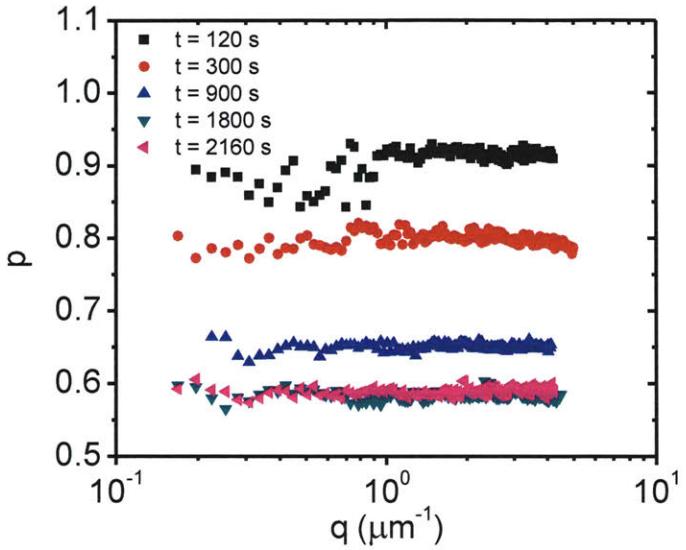

FIG. 4.15. Stretching exponent $p(q)$ of PS-PNIPAM gel of $\phi = 0.5\%$ at different times (legend) after the initiation of gelation ($T = 30°C$). The resulting p is largely independent of q over the entire range of length scales probed.

The evolution of $p(q)$ for the gels of three other volume fractions ($\phi = 0.3\%$, 0.8%, and 1.0%) at $T = 30°C$ exhibit identical features: q-independence, and gradual decrease with gel age. The rate of decrease, however, strongly depends on ϕ as displayed in Fig. 4.16 (a). As ϕ increases, p more rapidly saturates to a final value close to 0.6. For $\phi = 0.3\%$, p does not fall markedly below 1 until after the theoretical DLCA gelation time at 171 s (2.85 min), at which the uniformly sized clusters start to span the whole system space, and then gradually decreases to reach 0.6 at a later time. This delay, therefore, may evidence that the stretched exponential relaxation is a consequence of the kinetic arrest of the particles, regardless of the exact value of the stretching exponent p. For the samples with higher ϕ, the decrease in p follows the same trend, except for a shift to earlier times. For $\phi = 1.0\%$, the transition occurs too rapidly to be captured, and thus p reaches a plateau even before the first acquisition of the images at 120 s (2 min).

Similar to τ_{max} displayed in Fig. 4.13, these data points can be scaled in time as shown in Fig. 4.16 (b), except for $\phi = 1.0\%$, for which p is saturated already for the first image acquisition. This scaling again implies a time scale invariant behavior of aging. The horizontal shift factor as a

function of ϕ obeys a power law with exponent -2.85 as displayed in Fig. 4.17, close to the value found from the scaling of τ_{max} (-3.09) in Fig. 4.14. This strongly suggests a correlation between the evolution of $\tau(q)$ and $p(q)$. The physical origin of this correlation, however, currently remains an open question.

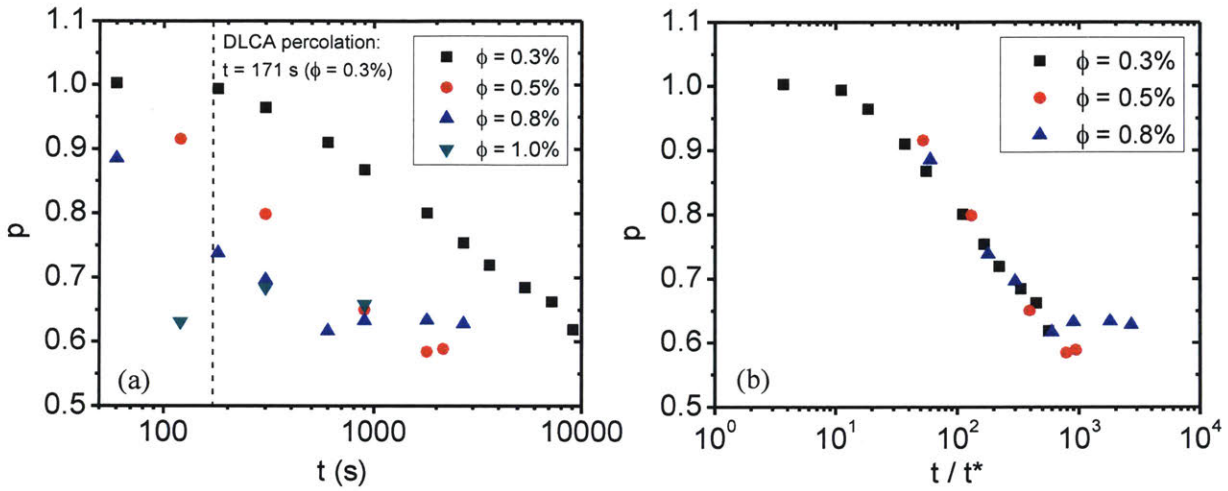

FIG. 4.16. (a) Temporal evolution of the stretching exponent p of PS-PNIPAM gel at different volume fractions ϕ (legend) after the initiation of gelation at $t = 0$ s ($T = 30$°C). The vertical dashed line indicates the gelation time (percolation) in the theoretical DLCA model for $\phi = 0.3\%$. (b) p in (a) shifted horizontally such that the decreasing parts for different ϕ fall onto a master curve.

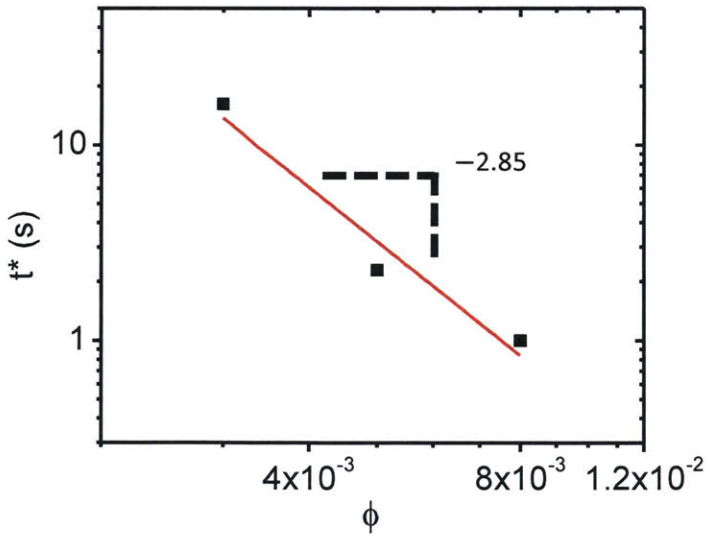

FIG. 4.17. Shift factors of p as a function of ϕ, as obtained from the scaling shown in Fig. 4.16 (b).

When multiple exponential relaxation modes constitute a stretched exponential relaxation, as in the Krall-Weitz model [11], the stretching exponent p contains complete information on the distribution of the relaxation time scales of the individual modes as studied by Johnston [40]. Then the gradual decrease of p during gelation from 1 to 0.6 may be a representation of the spreading distribution of single mode relaxation times from a delta function to a wide distribution with long tails of the fast relaxation modes driven by thermal fluctuations. Indeed, the exponent of 0.6 corresponds to the lowest maximum value and largest full width at half maximum of the density function of single mode relaxation times [40]. Furthermore, the spreading of the distribution may be attributed to intermittent break-up of bonds between highly agitated aggregates that can gradually cut out low frequency modes, while sustaining high frequency modes.

In this picture of the gel evolution, the fact that long-term p plateau is located at slightly lower magnitude for more dilute samples in Fig. 4.16 (a) is a corollary of missing the fastest relaxation modes in the images, because of the limited image acquisition frame rate. Further dilution of sample leads to faster motion of the smallest scatterers (e.g. individual particles), which in turn causes the camera to lose a greater amount of information on the fastest dynamics in the network. This loss manifests itself in the form of an underestimated exponent p, consistent with our results. The challenge lies in bringing this abstraction to the level of quantitatively supported argument when we can only obtain statistically averaged parameters.

Theoretically, the dynamic structure factor $f(q, \Delta t)$ of any vibrating fractal networks has been reported to decay as a stretched exponential with an exponent p, where the stretched exponential time scale $\tau(q)$ scales as $q^{-2/p}$ for large q [41]. This general relation between $\tau(q)$ and p indeed holds true in our colloidal gel networks, as shown in Fig. 4.18. For $\phi = 0.3\%$, the slope s_τ of the high q power law domain of $\tau(q)$ closely matches with the theoretical prediction of $-2/p$ for vibrating fractal networks. This agreement provides another sign of fractality of the PS-PNIPAM particle clusters, and indicates that p mirrors the distribution of relaxation times over multiple length scales.

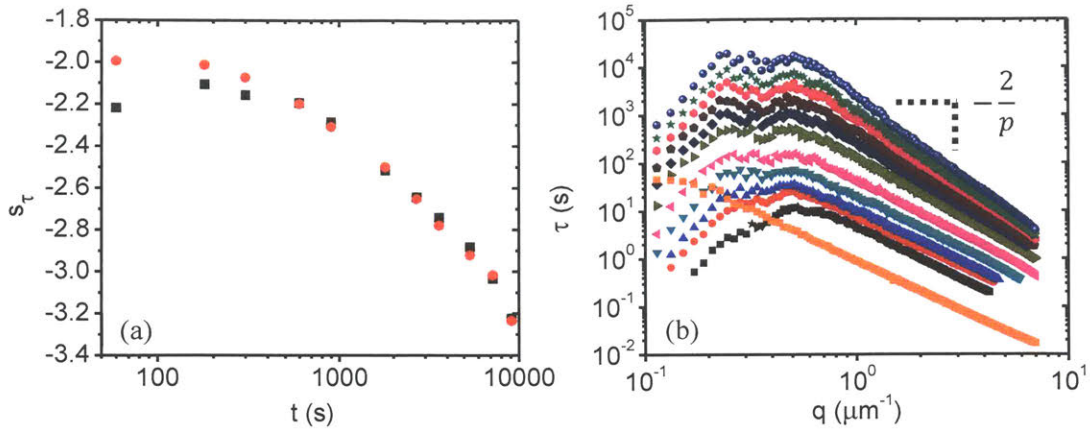

FIG. 4.18. (a) Slope (s_τ) of $\tau(q)$ in the high q-domain (black squares) and theoretical prediction ($-2/p$) of the power for vibrating fractals (red circles) based on the mean p values obtained from curve-fitting [41], as a function of the age of PS-PNIPAM colloidal gel ($\phi = 0.3\%$, $T = 30°C$). (b) $\tau(q)$ at different ages (shifted from the bottom to the top as the gel evolves) showing steeper slopes in the high q-domain for greater waiting time t.

4.3 Elasticity estimation using DDM

Quantitative exposition of the coupling between rheometric measurements and microscopic observations has been a task that has motivated many research groups [11,42–46]. Here, we develop our DDM analysis further to relate to rheology by estimating the elasticity of the gels with DDM parameters. We use the scaling prediction of the elastic shear modulus predicted by the Krall-Weitz model, which assumes that the macroscopic elasticity of the system is determined by the spring constant between adjacent clusters [11]. Since a shear strain unbends the network strands, rather than stretching them, the interaction among the largest units offers the floppiest mode in a multitude of normal modes that exist in the system. Hence, in the Krall-Weitz model, the shear modulus G scales as

$$G \sim \frac{\kappa_c}{R_c} = \frac{6\pi\eta b}{\tau^*}, \tag{4.3}$$

where κ_c is the inter-cluster spring constant, R_c the cluster radius, η the viscosity of background fluid, $b = 0.35$ a correction factor, and τ^* the q-independent characteristic relaxation time of the

mean square displacement used in Eq (3.1) [11]. The last expression clarifies that the modulus can be understood as the balance between Stokes drag in the numerator and displacement time scale in the denominator.

To obtain τ^* in the Krall-Weitz model from the DDM parameters, we compare the expressions for the dynamic structure factor $f(q,\Delta t)$ used. The functional form of $f(q,\Delta t)$, Eq (3.1), proposed in the Krall-Weitz model and here modified for 2D images is

$$f(q,\Delta t) = \exp\left[-\frac{q^2}{4}\delta^2\left\{1-\exp\left(-\left(\frac{\Delta t}{\tau^*}\right)^p\right)\right\}\right] \tag{4.4}$$

[11], while the simplified form we use for the DDM analysis on non-ergodic media is Eq (3.2) (repeated here)

$$f(q,\Delta t) = \big(1-C(q)\big)\exp\left[-\left(\frac{\Delta t}{\tau(q)}\right)^{p(q)}\right] + C(q). \tag{3.2}$$

Equating these two expressions for early delay time Δt yields

$$\frac{q^2}{4}\delta^2\left(\frac{\Delta t}{\tau^*}\right)^p \sim \left(\frac{\Delta t}{\tau(q)}\right)^p, \tag{4.5}$$

which then leads to

$$\tau^* \sim \frac{(q\delta)^{\frac{2}{p}}}{4^{\frac{1}{p}}}\tau(q), \tag{4.6}$$

where q and $\tau(q)$ are any set of values in the high q regime that probes the internal dynamics of clusters. Indeed, the power law of $\tau(q) \sim q^{-\frac{2}{p}}$ in the high q-domain discussed in section 4.2.4 renders τ^* in Eq. (4.6) q-independent.

The value of δ^2 can be found from $C(q)$ in Eq. (3.2), since in the limit of $\Delta t \to \infty$, equating the two expressions for $f(q,\Delta t)$ results in

$$\exp\left(-\frac{q^2}{4}\delta^2\right) = C(q). \tag{4.7}$$

Although rather noisy compared the other parameters such as $\tau(q)$ or $p(q)$, $C(q)$ as obtained by the method delineated in Chapter 3 provides a bell-shaped curve with its peak close to the limit of

$q \to 0$, as shown in Fig. 4.19, for the PS-PNIPAM colloidal gel of $\phi = 0.3\%$ and $T = 30°C$, during gelation.

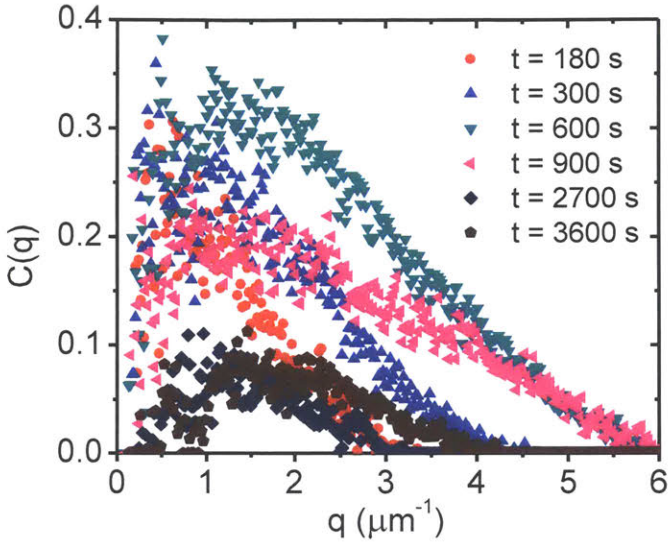

FIG. 4.19. $C(q)$ for PS-PNIPAM colloidal gels ($\phi = 0.3\%$, $T = 30°C$) at different gel ages (legend). Each of the data sets roughly follows the right half of a Gaussian-type curve as predicted by Eq (4.7).

By another curve-fitting optimization using Eq (4.7), with a correction factor multiplied to allow the y-intercept to be a value lower than 1, we compute the values of the maximum mean square displacement δ^2 in the gel network, and finally the shear modulus G using Eq (4.3). Both quantities are shown in Fig. 4.20 as a function of time after the initiation of gelation. Even though DDM captures reasonable values for δ^2 at the beginning of gelation, it quickly reaches a plateau while $\tau(q)$ in Eq. (4.6) continues to increase. This mismatch causes the estimated G value to dramatically decrease, in contrast to what we find in the rheometric measurements.

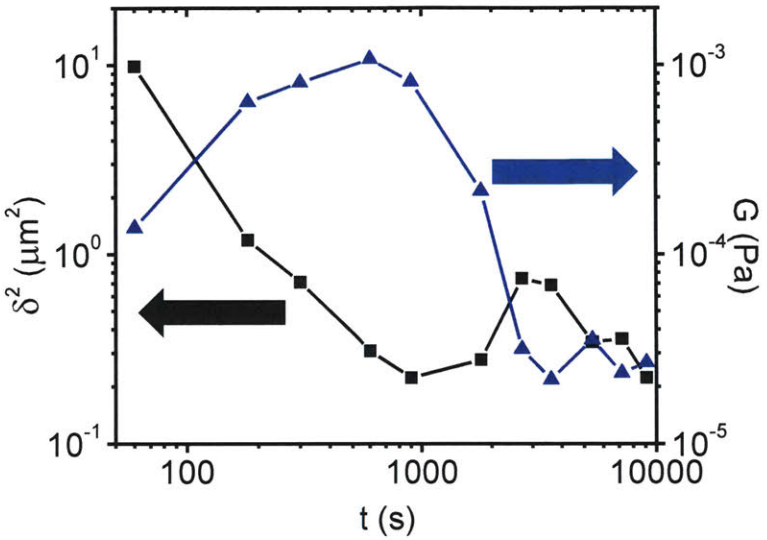

FIG. 4.20. Maximum mean square displacement δ^2 (black squares) of scatterers in the PS-PNIPAM gel network ($\phi = 0.3\%$, $T = 30°C$) and the corresponding estimation of shear modulus G (blue triangles). δ^2 saturates to a minimum while the dynamics continuously slow down, making the estimated G inaccurate for later ages. Lines are guides to the eye.

The saturation of δ^2 to the order of 0.1 μm^2 is most likely induced by the image resolution limit, whose pixel size in the real space is equivalent to 0.1 μm. A naïve scaling of the minimum δ^2 detected in DDM is 0.1 $\mu m \times 0.1$ $\mu m = 0.01$ μm^2, but noise in the actual data can easily raise the limit to the level observed in Fig. 4.20. Indeed, calculation of δ^2 from $C(q)$ of denser samples results in more rapid saturation to the values of the order 0.1 μm^2 or 0.01 μm^2.

Yet, this result provides valid values of G for the earliest stage of gelation. For the sample with $\phi = 0.3\%$ at $T = 30°C$, the estimate via DDM yields a G of $\sim 1.0 \times 10^{-3}$ Pa before the saturation due to the resolution limit. In comparison, G' of the fully evolved gel for the same volume fraction is extrapolated to be $\sim 7.9 \times 10^{-3}$ Pa from the power law reported in Fig. 4.5 (a). This extrapolated value of G' would indeed be a reasonable prediction of the plateau magnitude to be found in Fig. 4.20, if it were not for the resolution limit.

Whether we can justify this direct application of the Krall-Weitz framework to evolving systems remains to be answered. The model assumes independence among the oscillating scatterers at different length scales, which appears rather crude for a system whose viscoelastic properties are determined by the collective behavior of particles and their aggregates. The inter-cluster length scale dynamics newly presented by DDM may instead contain a key to predicting the bulk elasticity, accounting for the interaction among the oscillators.

4.4 Strengths and limitations of DDM analysis on colloidal gels

Compared to the conventional scattering techniques used on non-ergodic systems, DDM preserves all of its advantages discussed in Chapter 2 in its application to the colloidal gels: low cost, easy implementation, high throughput, and compatibility with multiply scattering samples. One of the most significant strengths of DDM in the analysis of heterogeneous, non-ergodic systems is that we can instantaneously access the ensemble-averaged information over multiple length scales, thus enabling us to holistically probe the structure and dynamics of the system during its transient state. In the low q-domain, therefore, DDM provides a detailed picture of the dynamics at the length scales larger than cluster sizes, revealing novel behaviors, which other localized probing techniques are blind to.

Use of DDM to analyze the microscopic dynamics of the PS-PNIPAM colloidal gels also uncovers several limitations. The most obvious technical limit of processing the images to calculate the image structure function is the computation cost. For an image stack file with $N = 1000$ frames of 2048×2048 pixels, the image structure function computation takes more than 7 hours, which substantially increases the analysis time. Although optimization of algorithm and the use of GPUs for parallel computing can reduce the computation cost, real-time calculation of the correlation function is not practical, especially in case of analyzing heterogeneous media such as colloidal gel networks, where extensive ensemble-averaging is crucial for statistical integrity.

Another practical limit to the DDM analysis, specifically for linking DDM parameters to rheological properties of the gels, lies on the narrow range of particle volume fraction that is compatible with microscopy. DDM allows us to examine samples at concentrations too high for DLS, where incident light has to be only singly scattered. Yet bright-field microscopy requires the sample to be sufficiently dilute to allow light to be transmitted through the sample. This restriction prevents us from measuring dynamics of samples of comparable ϕ with those mechanically measured on a rheometer.

A further limit to investigating dense samples can be ascribed to the low spatial and temporal resolution of DDM, compared to the sensitive detectors used in other light scattering apparatuses. Given a technical upper bound on the throughput, generating high definition images inevitably compromises the speed of imaging, which renders DDM insensitive to the fastest dynamics in the system. On the other hand, the number of pixels in the images determines the highest accessible wave vector q, and given a finite magnification of the objective, we cannot probe the smallest displacements of particle network segments. This technical limit seems to cause the estimation of the gel elasticity to be impractical, except for the very early stage.

Chapter 5

Tuning mechanical properties of colloidal gels: Binary mixture

The prime engineering value of understanding the connection between macroscopic mechanical properties and microscopic dynamics of soft materials is rooted in potential tunability of the systems. Our design strategy to reach such tunability in colloidal gels lies in the use of mixtures of two different types of particles: one characterized by strong attractive interactions ($U\sim 30\ k_BT$), the other by weak attractive interactions ($U \sim 5\ k_BT$). As seen in the evolution of G' and G'' of the two systems after the initiation of gelation at $t = 0$ s for $\phi = 5\%$ at $T = 30°C$ in Fig. 5.1, the moduli of the strong system, used so far in this work, are two orders of magnitude higher than those of the weak system. We now start to explore with rheology and DDM how mixtures of these two types of particles give rise to novel mechanical properties.

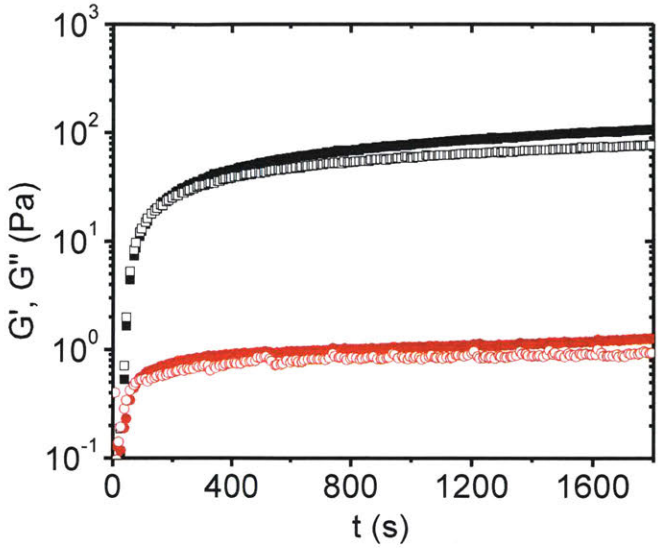

FIG. 5.1. Temporal evolution of G' (solid) and G'' (open) after the initiation of gelation at $t = 0$ s of the strong (black squares), and the weak (red circles) systems ($\phi = 5\%$, $T = 30°C$). The moduli between the two systems differ by two orders of magnitude.

Mixing the two systems at different ratios with total particle volume fraction $\phi = 5\%$ at $T = 30°C$ leads to a similar temporal evolution of the moduli as for the individual systems. To systematically investigate how the properties of the mixed systems vary with different mixing ratios, we alter the relative proportions of the two particles by volume, keeping the total volume fraction constant at $\phi = 5\%$. Gradually decreasing the proportion of the strong particles, we obtain gels with gradually decreasing moduli as shown in Fig. 5.2. Both the starting time of the initial sharp increase in the moduli and the time of crossover between G' and G'' remain similar for all gels.

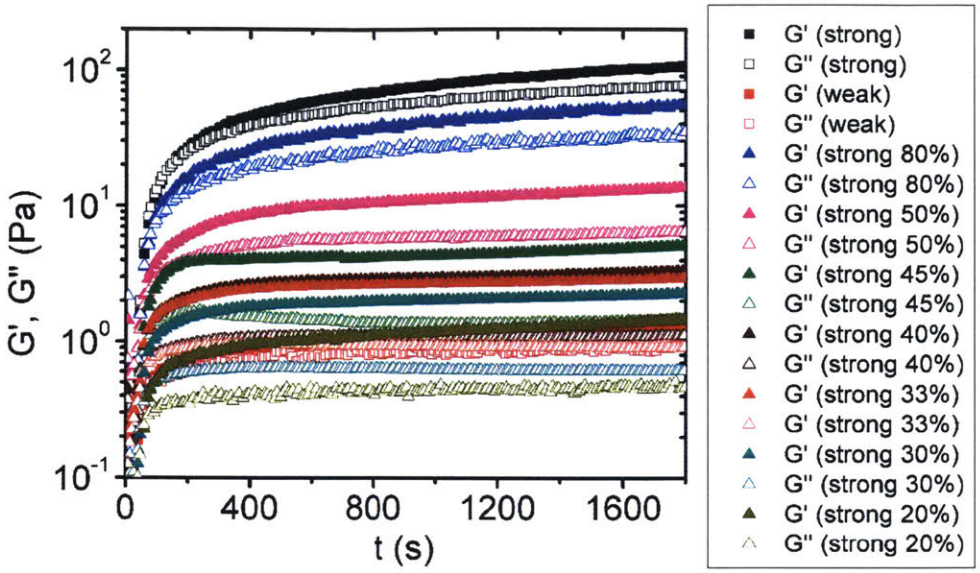

FIG. 5.2. G' and G'' of the mixtures of strong and weak PS-PNIPAM colloidal gels with different volume ratios (legend) ($\phi = 5\%$, $T = 30°C$) in the time sweep experiments. The moduli systematically increase over two orders of magnitude with the proportion of the strong particles. There is no obvious change in any time scale as a function of the ratio.

By contrast, we find that the yielding behavior of the gels exhibits drastically modified characteristics in the mixtures, as shown in Fig. 5.3 for the samples of $\phi = 5\%$ at $T = 30°C$. The strong gel alone displays a limit of linearity at $\gamma_0 \cong 8 \times 10^{-3}$. The weak gel, however, exhibits a much broader linear regime and a strain-hardening behavior before fracture. Remarkably, increasing the proportion of the strong particles in the mixture gradually erases the strain-hardening by inducing a nonlinear decrease of the moduli at lower strain amplitudes. In particular, the balance between these two types of nonlinearity leads to a double yielding behavior at intermediate proportions of strong and weak particles, where the gel retains the signatures of both.

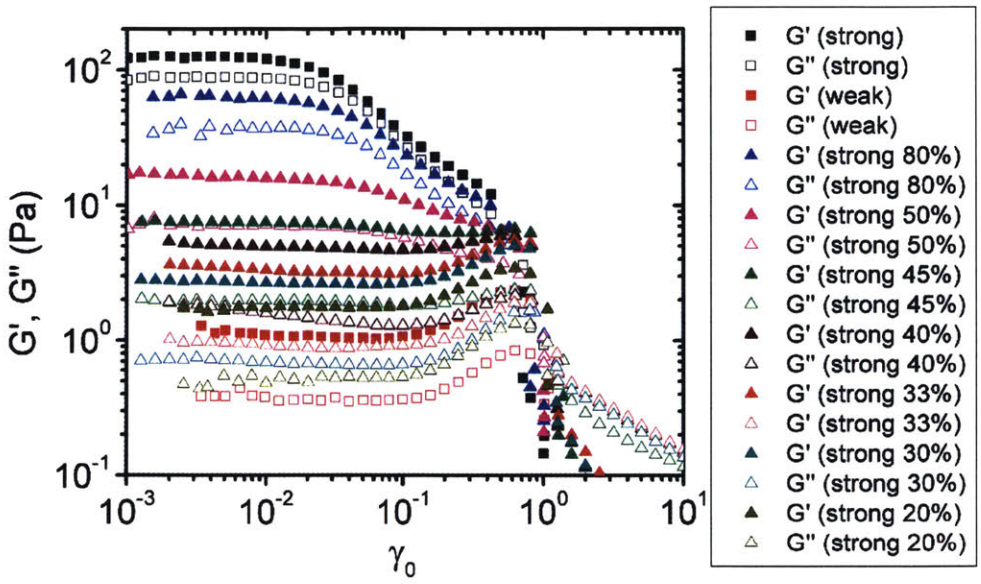

FIG. 5.3. G' and G'' of the mixture of strong and weak PS-PNIPAM colloidal gels with different volume ratios (legend) ($\phi = 5\%$, $T = 30°C$, gel age $t > 30$ min) in the strain sweep experiments. Not only does the magnitude of the moduli vary as a function of the ratio, but also the nonlinear behavior systematically changes by showing strain-hardening.

Strain-hardening has been ascribed to the stretching of the particle chains in the network that follows unbending of the chains as the strain amplitude increases [10]. While the strain-hardening is a result of chain stretching, moduli of the gels are measures of the resistance against chain bending. Therefore, this picture of strain-hardening explains the consistent final yielding strain amplitude, independent of the mixing ratio.

As the mixture gel becomes stiffer with increasing strong particle proportion, we speculate that the gel simultaneously grows brittle, which drives the earlier onset of nonlinearity before the strain-hardening regime. For the gels with intermediate ratios, consequently, signs of both modes of nonlinearity are observed in two separate steps, suggesting a possibility of tuning the large amplitude deformation behavior of colloidal gels. The double yielding behavior has been discussed in different rheological studies of colloidal gels [47], and we expect our experiments with the mixtures will contribute to a better understanding of the phenomenon.

Most strikingly, the frequency dependence of the viscoelastic moduli is highly sensitive to the interaction potential. While the strong system alone shows a relaxation within our experimental frequency window, the weak system alone displays a pronounced dominance of G' over the probed frequency domain. In the binary mixtures, the frequency behavior changes systematically with increasing proportion of the weak particles, as shown in Fig. 5.4 (a). This versatility in the frequency response of the PS-PNIPAM mixture gels becomes most evident when we scale the data sets onto a master curve, as in Fig. 5.4 (b).

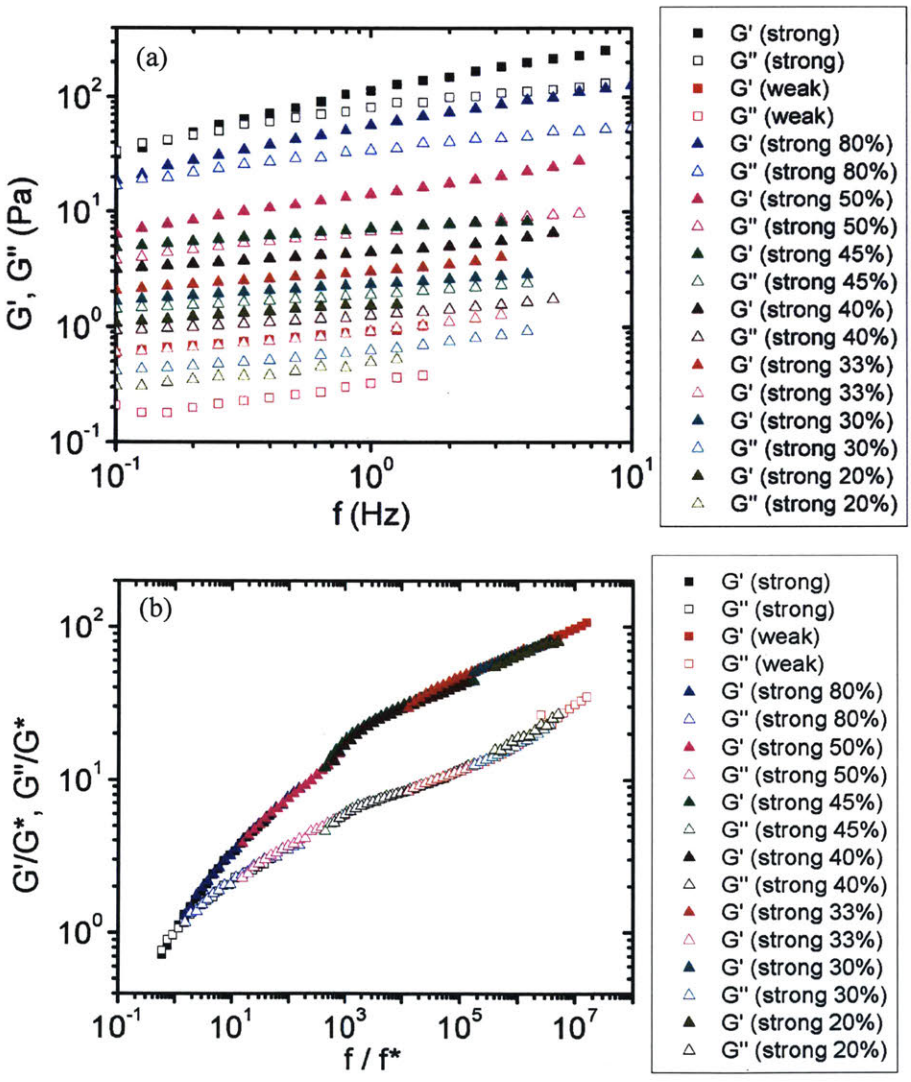

FIG. 5.4. (a) G' and G'' of the mixture of strong and weak PS-PNIPAM gels with different volume ratios (legend) ($\phi = 5\%, T = 30°C$, gel age $t > 30$ min) in the frequency sweep experiments. (b) A master curve obtained by scaling the data with respect to the crossover values. This scaling onto a master curve reveals a universality in the frequency response of the colloidal gels.

This master curve indicates that by adjusting the ratios of the particles, we can tune the relaxation time of the resulting gel that varies over an extraordinary range of seven orders of magnitude. Let us note that this frequency response is on a first sight rather counterintuitive. Our data clearly show that the relaxation time of a stronger gel is much faster than that of weaker gels – an intriguing result that warrants further investigation.

Our new DDM tools we have developed will allow us to explore this broad spectrum of relaxation dynamics seen in rheology in greater detail. DDM can effectively capture the increased heterogeneity in the dynamics introduced by mixing the two types of particles through its powerful ensemble-averaging algorithm over multiple length and times scales. Moreover, as the difference in the inter-particle potential sets the structural features of the space-spanning network, we expect to benefit from direct visualization of the network configuration by dying the two types of particles with different colors in confocal fluorescent microscopy. This study of the change in microscopic dynamics and structure accompanying the wide rheological variation will help us delineate a more universal picture of colloidal gels.

References

[1] P. Meakin, *Formation of Fractal Clusters and Networks by Irreversible Diffusion-Limited Aggregation*, Phys. Rev. Lett. **51**, 1119 (1983).

[2] M. Kolb, R.Botet, and R.Jullien, *Scaling of Kinetically Growing Clusters*, Phys. Rev. Lett. **51**, 1123 (1983).

[3] D. A. Weitz and M. Oliveria, *Fractal Structures Formed by Kinetic Aggregation of Aqueous Gold Colloids*, Phys. Rev. Lett. **52**, 1433 (1984).

[4] R. Jullien and M. Kolb, *Hierarchical Model for Chemically Limited Cluster-Cluster Aggregation*, J. Phys. A Gen. Phys. **17**, L639 (1984).

[5] D. A. Weitz, J. S. Huang, M. Y. Lin, and J. Sung, *Limits of the Fractal Dimension for Irreversible Kinetic Aggregation of Gold Colloids*, Phys. Rev. Lett. **54**, 1416 (1985).

[6] R. C. Ball, D. A. Weitz, T. A. Witten, and F. Leyvraz, *Universal Kinetics in Reaction-Limited Aggregation*, Phys. Rev. Lett. **58**, 274 (1987).

[7] W.-H. Shih, W. Shih, S.-I. Kim, J. Liu, and I. Aksay, *Scaling Behavior of the Elastic Properties of Colloidal Gels*, Phys. Rev. A **42**, 4772 (1990).

[8] M. Carpineti and M. Giglio, *Spinodal-Type Dynamics in Fractal Aggregation of Colloidal Clusters*, Phys. Rev. Lett. **68**, 3327 (1992).

[9] J. P. Pantina and E. M. Furst, *Elasticity and Critical Bending Moment of Model Colloidal Aggregates*, Phys. Rev. Lett. **94**, 8 (2005).

[10] T. Gisler, R. C. Ball, and D. A. Weitz, *Strain Hardening of Fractal Colloidal Gels*, Phys. Rev. Lett. **82**, 1064 (1999).

[11] A. H. Krall and D. A. Weitz, *Internal Dynamics and Elasticity of Fractal Colloidal Gels*, Phys. Rev. Lett. **80**, 778 (1998).

[12] L. Cipelletti, S. Manley, R. C. Ball, and D. A. Weitz, *Universal Aging Features in the Restructuring of Fractal Colloidal Gels*, Phys. Rev. Lett. **84**, 2275 (2000).

[13] R. Cerbino and V. Trappe, *Differential Dynamic Microscopy: Probing Wave Vector Dependent Dynamics with a Microscope*, Phys. Rev. Lett. **100**, 1 (2008).

[14] N. Dingenouts, C. Norhausen, and M. Ballauff, *Observation of the Volume Transition in Thermosensitive Core−Shell Latex Particles by Small-Angle X-Ray Scattering*, Macromolecules **31**, 8912 (1998).

[15] K. Kubota, S. Fujishige, and I. Ando, *Solution Properties of Poly(N-Isopropylacrylamide) in Water*, Polym. J. **22**, 15 (1990).

[16] Y. Kantor and I. Webman, *Elastic Properties of Random Percolating Systems*, Phys. Rev. Lett. **52**, 1891 (1984).

[17] R. H. Ewoldt, M. T. Johnston, and L. M. Caretta, *Experimental Challenges of Shear Rheology: How to Avoid Bad Data*, in *Complex Fluids Biol. Syst.* (Springer, New York, 2015), pp. 207–241.

[18] B. Costello, *The AR-G2 Magnetic Bearing Rheometer* (2005).

[19] M. Reufer, V. A. Martinez, P. Schurtenberger, and W. C. K. Poon, *Differential Dynamic Microscopy for Anisotropic Colloidal Dynamics*, Langmuir **28**, 4618 (2012).

[20] F. Giavazzi, S. Crotti, A. Speciale, F. Serra, G. Zanchetta, V. Trappe, M. Buscaglia, T. Bellini, and R. Cerbino, *Viscoelasticity of Nematic Liquid Crystals at a Glance*, Soft Matter **10**, 3938 (2014).

[21] A. Jepson, V. A. Martinez, J. Schwarz-Linek, A. Morozov, and W. C. K. Poon, *Enhanced*

Diffusion of Nonswimmers in a Three-Dimensional Bath of Motile Bacteria, Phys. Rev. E **88**, 3 (2013).

[22] M. Drechsler, F. Giavazzi, R. Cerbino, and I. M. Palacios, *Active Diffusion and Advection in Drosophila Oocytes Result from the Interplay of Actin and Microtubules*, Nat. Commun. **8**, (2017).

[23] P. Edera, D. Bergamini, V. Trappe, F. Giavazzi, and R. Cerbino, *Differential Dynamic Microscopy Microrheology of Soft Materials: A Tracking-Free Determination of the Frequency-Dependent Loss and Storage Moduli*, Phys. Rev. Mater. **073804**, 1 (2017).

[24] A. V Bayles, T. Squires, and M. E. Helgeson, *Dark-Field Differential Dynamic Microscopy*, Soft Matter **12**, 2440 (2016).

[25] P. J. Lu, F. Giavazzi, T. E. Angelini, E. Zaccarelli, F. Jargstorff, A. B. Schofield, J. N. Wilking, M. B. Romanowsky, D. A. Weitz, and R. Cerbino, *Characterizing Concentrated, Multiply Scattering, and Actively Driven Fluorescent Systems with Confocal Differential Dynamic Microscopy*, Phys. Rev. Lett. **108**, 1 (2012).

[26] K. He, M. Spannuth, J. C. Conrad, and R. Krishnamoorti, *Diffusive Dynamics of Nanoparticles in Aqueous Dispersions*, Soft Matter **8**, 11933 (2012).

[27] R. Cerbino and P. Cicuta, *Perspective: Differential Dynamic Microscopy Extracts Multi-Scale Activity in Complex Fluids and Biological Systems*, J. Chem. Phys. **147**, 110901 (2017).

[28] E. Zaccarelli, *Colloidal Gels: Equilibrium and Non-Equilibrium Routes*, J. Phys. Condens. Matter **19**, 323101 (2007).

[29] P. N. Pusey and W. van Megen, *Dynamic Light Scattering by Non-ergodic Media*, Physica A **157**, 705 (1989).

[30] J. Z. Xue, D. J. Pine, S. T. Milner, X. L. Wu, and P. M. Chaikin, *Nonergodicity and Light Scattering from Polymer Gels*, Phys. Rev. A **46**, 6550 (1992).

[31] F. Giavazzi and R. Cerbino, *Digital Fourier Microscopy for Soft Matter Dynamics*, J. Opt. **16**, 083001 (2014).

[32] J. L. Arauz-Lara, *Colloidal Fluids*, in *Fluids, Colloids Soft Mater. An Introd. to Soft Matter Phys.* (John Wiley & Sons, Inc., 2016), pp. 189–201.

[33] L. Cipelletti, V. Trappe, and D. J. Pine, *Scattering Techniques*, in *Fluids, Colloids Soft Mater. An Introd. to Soft Matter Phys.* (John Wiley & Sons, Inc., 2016), pp. 133–148.

[34] R. J. M. d'Arjuzon, W. Frith, and J. R. Melrose, *Brownian Dynamics Simulations of Aging Colloidal Gels*, Phys. Rev. E **67**, 061404 (2003).

[35] L. Cipelletti, L. Ramos, S. Manley, E. Pitard, D. A. Weitz, E. E. Pashkovski, and M. Johansson, *Universal Non-Diffusive Slow Dynamics in Aging Soft Matter*, Faraday Discuss. **123**, 237 (2002).

[36] A. H. Krall, Z. Huang, and D. A. Weitz, *Dynamics of Density Fluctuations in Colloidal Gels*, Physica A **235**, 19 (1997).

[37] E. Del Gado, D. Fiocco, G. Foffi, S. Manley, V. Trappe, and A. Zaccone, *Colloidal Gelation*, in *Fluids, Colloids, Soft Mater. An Introd. to Soft Matter Phys.* (2016), pp. 279–290.

[38] R. B. Bird, R. C. Armstrong, and O. Hassager, *The General Linear Viscoelastic Fluid*, in *Dyn. Polym. Liq. Vol. 1 Fluid Mech.*, 2nd ed. (Wiley, 1987), pp. 255–290.

[39] S. Romer, F. Scheffold, and P. Schurtenberger, *Sol-Gel Transition of Concentrated Colloidal Suspensions*, Phys. Rev. Lett. **85**, 4980 (2000).

[40] D. C. Johnston, *Stretched Exponential Relaxation Arising from a Continuous Sum of*

Exponential Decays, Phys. Rev. B **74**, 1 (2006).

[41] S. Reuveni, J. Klafter, and R. Granek, *Dynamic Structure Factor of Vibrating Fractals*, Phys. Rev. Lett. **108**, 1 (2012).

[42] M. B. Gordon, C. J. Kloxin, and N. J. Wagner, *The Rheology and Microstructure of an Aging Thermoreversible Colloidal Gel*, J. Rheol. (N. Y. N. Y). **61**, 23 (2017).

[43] Q. Zhang, D. Bahadur, E. M. Dufresne, P. Grybos, P. Kmon, R. L. Leheny, P. Maj, S. Narayanan, R. Szczygiel, S. Ramakrishnan, and A. Sandy, *Dynamic Scaling of Colloidal Gel Formation at Intermediate Concentrations*, Phys. Rev. Lett. **119**, 1 (2017).

[44] S. Romer, H. Bissig, P. Schurtenberger, and F. Scheffold, *Rheology and Internal Dynamics of Colloidal Gels from the Dilute to the Concentrated Regime*, Europhys. Lett. **108**, 1 (2014).

[45] H. Guo, S. Ramakrishnan, J. L. Harden, and R. L. Leheny, *Gel Formation and Aging in Weakly Attractive Nanocolloid Suspensions at Intermediate Concentrations*, J. Chem. Phys. **135**, (2011).

[46] A. Zaccone, H. H. Winter, M. Siebenbürger, and M. Ballauff, *Linking Self-Assembly, Rheology, and Gel Transition in Attractive Colloids*, J. Rheol. (N. Y. N. Y). **58**, 1219 (2014).

[47] N. Koumakis and G. Petekidis, *Two Step Yielding in Attractive Colloids: Transition from Gels to Attractive Glasses*, Soft Matter **7**, 2456 (2011).